UNIVERSITY OF TWENTE.

Faculty of Electrical Engineering,
Mathematics & Computer Science

GaN Based Higher Power Inductive Transfer System for E-bikes

Remigius B. Jonkman

M.Sc. Thesis
January 19, 2022

Supervisors:
dr.ir. P. Venugopal (Prasanth)
dr.ir. C. Salm (Cora)

Power Electronics and EMC Group
Faculty of Electrical Engineering,
Mathematics and Computer Science
University of Twente
P.O. Box 217
7500 AE Enschede
The Netherlands

Summary

The past years an evolution has been ongoing in the field of transportation. Cars, scooters, steps, bikes anything and everthing that moves is electrified. On the side, there has also been a significant rise in shared transportation leading to a hazzle when it comes to charging. These shared vehicles would ideally be charged when parked in the easiest, cheapest and fastest way possible. Wireless power transfer is one of the technologies to fulfill these requirements. It is for this reasoning that a 1kW system is presented that is load-independent and can reach efficiencies of up to 90% in simulation.

The study starts with an introduction to new technologies in power electronics such as galium-nitride and silicon-carbide semiconductor devices. Alongside, the basics of the system are introduced from coupling to switching techniques as a way to prepare the reader for the next chapters.

The characteristics of S-S, LCL-P and LCL-LCL are presented and compared as part of system design. This is built up from the simplest LC networks to gain insight. Both S-S and LCL-LCL are very similar and act purely resistive, whereas LCL-P reflects a capacitive reactance to the primary. For all resonant networks the expressions for optimum load resistance as well as link efficiency are derived. This was calculationally complex for LCL-P and LCL-LCL, which is probably why it could not be found in literature.

Eventually a system is designed in which the link is modelled in FEM software to study the effects of misalignment and find the optimum coupler. The class-E inverter is set out to be completely load-independent to have the best performance for varying coil orientations. Simulations of the full system show efficiencies of up to 90% with an output power in the vicinity of $1\,\mathrm{kW}$. The full design was simulated and tested. Experimental results as validation are supplied as well, yielding $52\,\mathrm{W}$ output power at 70% efficiency.

Contents

Acronyms

WPT	wireless power transfer
IPT	inductive power transfer
NIR	non-ionizing radiation
ICNIRP	International Commission on Non-Ionizing Radiation Protection
CMT	coupled mode theory
WPC	Wireless Power Consortium
FOM	figure of merit
SS	series-series
LCL-P	LCL primary, parallel secondary
LCL-LCL	double-sided LCL
FEM	finite element method
ZCS	zero current switching
ZVS	zero voltage switching
ZVdS	zero voltage derivative switching
ISM	industrial, scientific and medical
2DEG	two degree electron gas

Chapter 1

Introduction

The e-mobility market is booming and everyone knows it. The most apparent market worldwide is currently electric cars, but there is also rising interest in other types of e-mobility. Especially in flat countries, such as the Netherlands, people have the habit of grabbing the electric bike to zigzag through the city and get to their destination quick and easy. Where traditionally people owned their own means of transport, a shift is occuring towards sharing. This not only saves you initial costs and maintenance, it is also a good deed climate wise. However, when it is electric, there is one major issue: it runs on batteries. Consequently, the company you rent from must provide a means to charge it at their parking spot. For a long time, they used mechanical contraptions to do so, requiring a lot of space, weight and maintenance (both at the parking spot and on the bike). Recent advances in wireless power transfer (WPT) show it can be done differently, a bike can be charged wirelessly. Providing an easier, cheaper, safer and at least as efficient means of charging.

With this application in mind, a $1\,\mathrm{kW}$ wireless charger utilizing resonant inductive power transfer is presented here. The system consists of a soft-switched load-independent class E inverter and an LCL-LCL link with passive rectifier. The load-independent inverter is designed to yield high performance even when coupling changes. To get the highest performance out of small electronics, the operational frequency is $6.78\,\mathrm{MHz}$ requiring the usage of GaN FETs and SiC schottky diodes.

1.1 Research Objectives

This thesis is set out to investigate inductive WPT with the main goal to develop a high efficiency 1kW wireless charging system for e-bikes over a distance of 5 centimers with potential misalignments of 1 centimeter. Ultimately, there should be a concurrent wireless communication interface between the charger and receiver sharing the same magnetic structure. Several intermediate tasks are set out in order to fulfill this research project.

- Design and optimize the inductive link with help of finite element method (FEM) software
- Study resonant converters for high frequency and high efficiency applications
- Perform analysis of several resonant networks, namely series-series (SS), LCL primary, parallel secondary (LCL-P) and double-sided LCL (LCL-LCL) and choose one
- Design a circuit to support charging at 1kW
- Realize a lab-scale demonstrator to verify the theoretical results with experiments

1.2 Thesis Outline

Chapter two introduces terminology as well as fundamental background knowledge required to interpret this thesis. In chapter three, a literature research is presented discussing advances in the field. An analysis of S-S, LCL-P and LCL-LCL resonant networks as well as an introduction to inductive power transfer is found in chapter four. Chapter five shows the usage of FEM as a tool to parametrize your design and find an optimal resonator structure for the requirements. Next, in chapter six, the high-level design is presented followed by an explanation of the various sub-components. The simulation models are presented in chapter seven to validate theoretical findings. The results are discussed in chapter eight. This study is evaluated and concluded in chapter nine.

Chapter 2

Fundamentals

2.1 Inductive Coupling

Ampere's Law shows a relation between a current carrying conductor and the magnetic field around it. Assuming a straight circular conductor, the magnetic field H forms concentric circles around the wire of equal magnitude. The magnitude falls rapidly when the distance to the wire is increased.
In inductors the wire is arranged in closed loops in air or around a magnetic material. Due to Lenz's Law, a varying field inside the inductor causes a voltage (back-emf) in the inductor opposing the source. The back-emf is calculated via Faraday's Law:

$$\epsilon = -\frac{\partial \Phi}{\partial t} \tag{2.1}$$

where ϕ is the flux and ϵ is the back-emf voltage. Inductance is defined as the flux inside an inductor per unit of current. When the inductor generates this by itself, it is named self-inductance, $L_{self} = \Phi_{self}/I_{self}$. It is also possible for another flux-source (other inductor) to generate the flux. The result is the same, a voltage is induced. The name for this is the mutual inductance and is given as $M = \Phi/I_{other}$, where I_{other} is the current in the other inductor. A graphical representation of two cross coupled coils is depicted in figure 2.1. Another way to express mutual inductance is via equation 2.2. k is the coupling factor and is a number between bounded between 0 and 1. Inductors are ideally lossless and store reactive energy in their magnetic field.

$$M = k\sqrt{L_1 L_2} \tag{2.2}$$

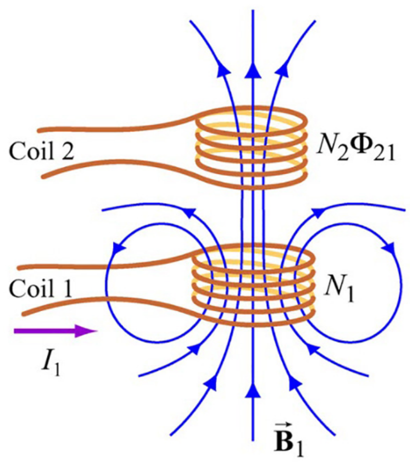

Figure 2.1: *Graphical representation of two coils with interactacting fluxes [1]*

2.2 Field Regions

The distance between the transmitter and receiver plays an important role in the received power and field magnitude near the receiver. To show this a current loop (magnetic loop antenna) in air is considered. The size of the loop is small compared to the frequency, so that the loop approximately carries a uniform sinusoidal current defined as $I = I_0 e^{j\omega t}$. Using polar coordinates, it is possible to express the magnetic fields as [2]:

$$H_\theta = \frac{m_0 \sin\theta e^{j(\omega t - \beta r)}}{4\pi}\left[\frac{-\beta_0^2}{r} + j\frac{\beta_0}{r^2} + \frac{1}{r^3}\right] \tag{2.3}$$

$$H_r = \frac{m_0 \cos\theta e^{j(\omega t - \beta r)}}{4\pi}\left[j\frac{\beta_0}{r^2} + \frac{1}{r^3}\right] \tag{2.4}$$

in these, m_0 is the magnetic moment, equal to $I_0 \pi a^2$ and β_0 is defined as the phase constant of free space and is equal to $2\pi/\lambda_0$. Conventionally, the terms in the magnetic field intensities are described as follows [2]:

1. $1/r$, radiation component in the far-field. The radiated far field power is independent of the distance between transmitter and receiver.

2. $1/r^2$, induction component in the radiating near-field. This part of the field is responsible for reactive energy storage.

3. $1/r^3$, magnetostatic component in the reactive near-field. The magnetic field is higly dominant.

The boundaries between these regions are loosely defined as $\lambda/2\pi$ and 2λ. This is also graphically shown in figure 2.2.

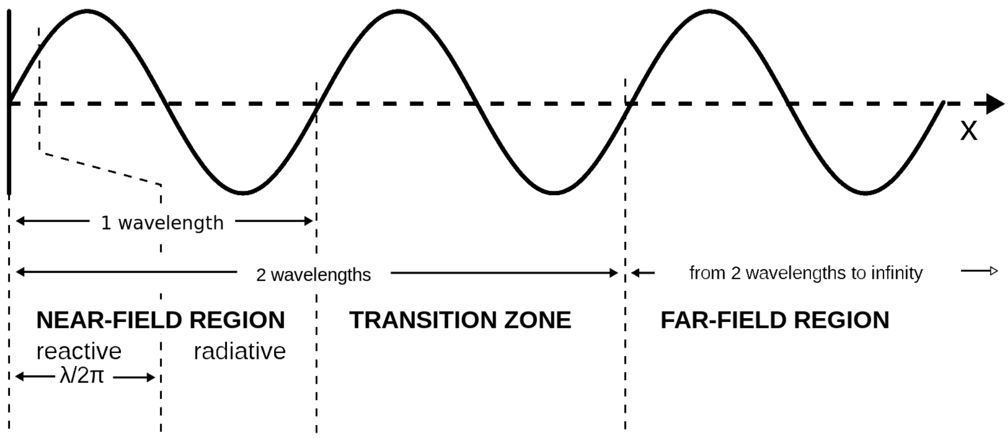

Figure 2.2: *Graphical representation of the field region boundaries [Image from Wikipedia]*

2.3 Semiconductor Materials

Most medium-to-low power designs currently utilize MOSFETS. However, the emergence of wide bandgap semiconductors such as siliconcarbide (SiC) and gallium-nitride (GaN) has diversified the choices for a designer. Table 2.1 shows key material characteristics. Based on this, it can be concluded that silicon is best suited for relatively low voltage applications, since the material has a small bandgap resulting in lower breakdown field strengths for equal material thicknesses. Silicon carbide devices are suited for high voltage and high power devices owing to their excellent thermal conductivity compared to Si and GaN. Additionally, the channel conductivity is lower than silicon due to the electron mobility, but a lot less dependent on temperature. Devices with the highest channel conductivity, highest switching speeds and breakdown voltages are GaN. These positive characteristics are all inherited from the high electron mobility, low parasitic capacitance and high bandgap. A serious disadvantage is the low thermal conductivity.

	Si	**SiC**	**GaN**
Bandgap Type	Indirect	Indirect	Direct
Bandgap $[eV]$	1.1	3.2	3.4
Breakdown Field Strength $[\frac{MV}{cm}]$	0.3	3.5	3.3
Electron Mobility $[\frac{cm^2}{Vs}]$	1500	650	2000
Thermal Conductivity $[\frac{W}{cmK}]$	1.5	5	1.3

Table 2.1: *Comparison between several semiconductor material properties*

2.4 GaN FETs

The channel of GaN FETs is formed by a two degree electron gas (2DEG). The conductivity of this channel is modulated through the gate that has a slight offset in the direction of the source. Apart from that, the device is symmetrical in the lateral direction. A schematic representation is given in figure 2.3a. The 2DEG is indicated by a small arrow. First quadrant operation of these devices is similar to silicon devices. Third quadrant operation is different as the drain and source swap. Usually, the threshold voltage is also different compared to the first quadrant, such that the device operates like a diode. First and third quadrant operation are graphically shown in figure 2.3b. The blue line depicts first quadrant operation, whereas the red line shows third quadrant operation. The benefits of GaN FETs in comparison to their silicon counterparts are, they:

- have zero reverse recovery losses as there is no intrinsic body diode
- are intrinsically capable of reverse current conduction
- are by default depletion mode devices. Enhancement mode devices are currently available as well
- require less switching energy
- allow for faster switching speeds
- have high breakdown voltages

Disadvantages of GaN FETs are their susceptibility to EMI, causing the gate to breakdown. Additionally, the thermal performance is lower compared to silicon.

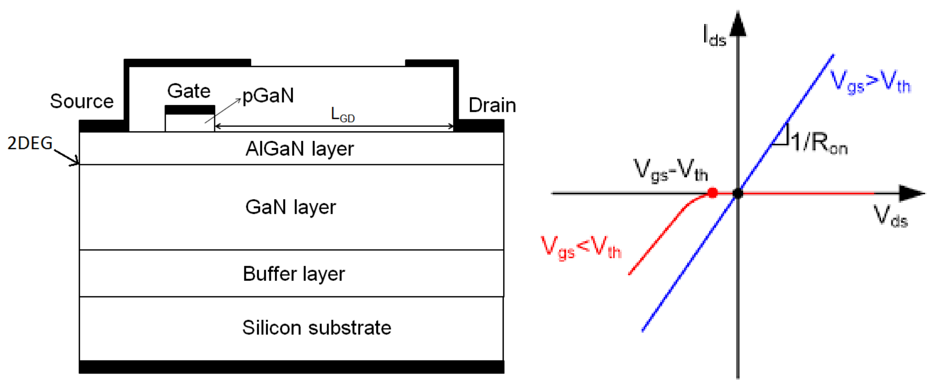

(a) *Lateral Structure [3]*   ***(b)*** *Operating Regions*

Figure 2.3: *GaN FET*

2.5 SiC Schottky Diodes

Another wideband semiconductor device that is frequently used in power electronics. The lateral structure is depicted in figure 2.4. Benefits of SiC schottky diodes compared to Si are:

- improved thermal performance
- increased breakdown voltages possible
- faster switching speeds

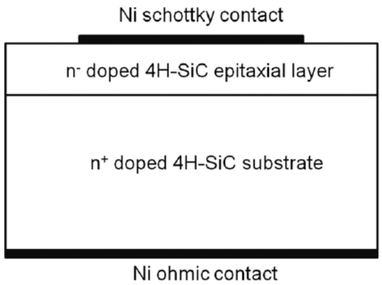

Figure 2.4: *SiC schottky diode lateral structure*

2.6 Losses

Losses in the resonator structure originate in the inductor and capacitor. The loss mechanisms are winding losses, iron losses, radiation losses and dielectric losses. In multi megaherzt designs, winding losses are usually dominant in WPT designs [4]. A quick review on the loss mechanims is given below.

- **Iron**: these are the total losses related to hysteresis and eddy currents in the soft magnetic core. An approximation is given in the Steinmetz equation [5] with the core loss density defined as: $k f_s^a \left[\Delta B_{max}\right]^b$, where k, a, b are calculated from the B-H hysteresis curve of the material, ΔB_{max} is the peak magnetic flux density and f_s is the switching frequency.
  - *Hysteresis*: the magnetic domains are expanded and contracted resulting in heat dissipation. These loss source is only available for inductors with magnetic cores.
  - *Eddy currents*: a changing magnetic field perpendicular to a conductor induces a current within due to Faraday's Law of Induction. The resistivity of the material and the induced current define the loss.
- **Winding**: these are the losses associated to current carrying conductors.
  - *Skin Effect*: due to eddy currents within a current carrying conductor, the current is concentrated around the outer periphery of the conductor. The skin depth, δ is given as: $\delta = \sqrt{\rho/\left(\pi f_s \mu\right)}$ with ρ as resistivity, μ as the material permeability. A decrease of one δ means a decline in current density of approximately 37%. A useful rule-of-thumb is that 98% of current flows within 4δ.
  - *Proximity Effect*: current carrying conductors that are in close prximity to eachother can cause irregular distribution of current densities, further increasing the AC resistance.
- **Radiation**: the power associated to the radiated far field energy. For structures that are very small compared to the wavelength, the consumed power is related to the radiation resistance: $R_{rad} = 20\pi^2 N^2 \left(\frac{l}{\lambda}\right)^4$ with N as the number of turns, l as the total winding length and λ as the wavelength.
- **Dielectic Losses**: capacitors have non-negligible losses for high frequency AC currents. The source of loss is the work done by the alternating electic field in re-orienting the dipoles.

2.6.1 Switch Losses

Ideal circuit models of switches typically have zero resistance when in the ON (closed) state and infinite resistance when in the OFF (open) state and are able to transition instantaneously between states. Addtionally there are no stray inductances or capacitances associated with a switch. All these assumptions implicitly make the switch a lossless component. In practice this does not hold due to the nature of semiconductor switches. The channel resistance is not zero resulting in conduction losses when in the ON state. Moreover, switches certainly cannot transition instantaneously resulting in transition losses. Together with losses due to stray capacitances and inductances, these losses are termed switching losses. The losses generate heat in the junction of the switch. Precautions are therefore required to ensure the thermals remain below the breakdown temperature. Additionally, thermal management is crucial for reliability and longevity of the device. Loss minimization and cooling is thus sensible.

2.6.1.1 Conduction Losses

In power applications semiconductor switches are ON when they operate in the ohmic region. In this operating region a small channel resistance $R_{DS,on}$ remains. The channel resistance is directly related to the applied gate voltage. Knowing the I_{sw} and channel resistance $R_{DS,on}$, the losses are accordingly calculated with the power law. In the OFF state the conduction losses are negligible.

2.6.1.2 Switching Losses

Semiconductor switches based on Si, SiC or GaN cannot transition instantenously, yielding an overlap between switch current and voltage, thus incurring losses. Additionally, there are losses in the output capacitance C_{oss}, gate capacitance C_G and reverse-conduction.

Transitions

The dominant mechanism in switching losses is typically the transition loss. Their loss mechanism is best explained when looking at a typical gate-charge curve for a GaN FET as in figure 2.5a. Several charge levels are indicated, namely:

- Q_{GS1} the charge required to get the gate to the threshold voltage and activate the device
- Q_{GS2} the charge necessary to commutate the current
- Q_{GD} the flat plateau is also known as the miller plateau. This cumulative charge is required to commutate the device voltage and reach the linear region
- Q_G the total charge that is concentrated in the gate and determines the device characteristics

The gate current magnitude determines the rise and fall times and therefore the speed of commutation and losses. Figure 2.5b indicates the rise and fall times graphically for an increasing gate voltage. An approximation of the loss during switch on transition is [6, 7]:

$$P_{trans,ON} = \frac{1}{2}\left(t_{cr} + t_{vf}\right) V_{BUS} \cdot I_{DS} \cdot f_{sw} \tag{2.5}$$

The turn off losses are calculated simarly:

$$P_{trans,OFF} = \frac{1}{2}\left(t_{vr} + t_{cf}\right) V_{BUS} \cdot I_{DS} \cdot f_{sw} \tag{2.6}$$

Another way to look at transition losses is to recognize the operating regions. During the transition, the switch jumps from saturation region to linear region or vice-versa. In the saturation region the switch conducts a large current and sustains a large voltage drop, thus incurring large losses.

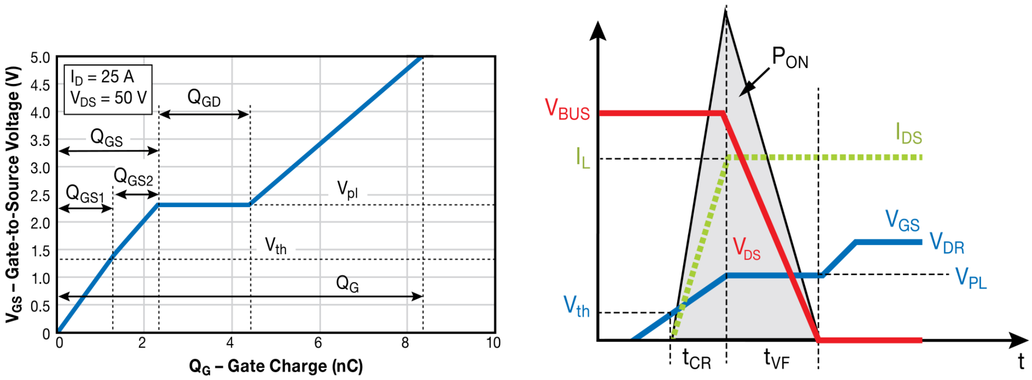

(a) Typical gate charge curve for a GaN FET *(b) Graphical representation of switching losses*

Figure 2.5: *Images are the courtesy of [7]*

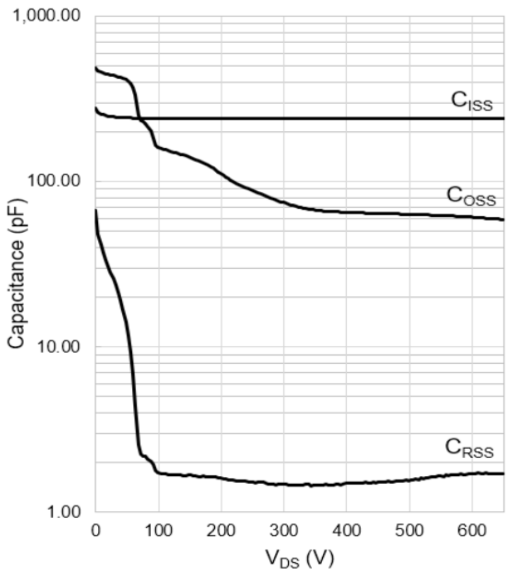

Figure 2.6: *GAN Systems GS66508B enhanced-mode GaN FET capacitances versus drain-source voltage*

Output Capacitance

Switches suffer additional losses due to the output capacitance, C_{oss}. This capacitance is highly nonlinear and dependent on the drain-source voltage. When the application is hard-switched, the accumulated charge in the output capacitance is quickly dissipated in the channel when the device turns on. The energy stored in the capacitance, E_{oss}, is therefore fully dissipated. The losses are also proportional to the switching frequency.

$$P_{oss} = f_{sw} E_{oss} \tag{2.7}$$

Gate Capacitance

Similarly, the gate capacitance is also continuously charged and discharged. This charge is generally not recycled and therefore a direct loss mechanism as well. Knowing the charge Q_G required to operate the switch, the gate loss power is:

$$P_G = Q_G f_{sw} \left(V_{GS,on} - V_{GS,off} \right) \tag{2.8}$$

Reverse Conduction

As already explored in section 2.4, reverse conduction in GaN FETs is inherently possible. The behavior is similar to a diode with the corresponding losses as well.

2.7 Switching Techniques

Switching inverters are traditionally operated in hard-switched mode, meaning that all of the above mechanisms combined define the total loss inside the switch. The performance of applications requiring a high power and high frequency therefore deteriorates. Soft switching was introduced to reduce switching losses and switch stresses. The main idea behind soft switching is surprisingly simple: 'during transitions either the voltage of current is zero.' This resulted in two techniques, namely zero current switching (ZCS) and zero voltage switching (ZVS).

Zero Current Switching

Turn-off transitions are improved with ZCS. Before switching, the current is ideally reduced to zero (see figure 2.7a). The improvement compared to hard-switching is marginal. The output voltage is kept low due to the output capacitance [6] when hardswitching. Thus already reducing the transition losses.

Zero Voltage Switching

In contrast with ZCS, ZVS improves the turn-on efficiency. Before transitioning, the output capacitance is discharged and the switch voltage is reduced to zero (see figure 2.7b). An additional benefit is a faster switching time as there is no charge required to discharge the gate-drain capacitance. In FETs, ZVS is superior to ZCS.

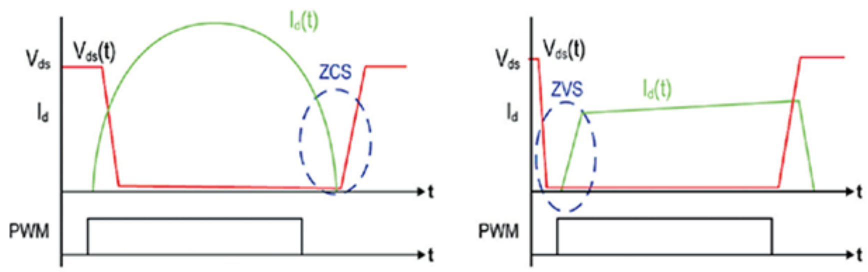

(a) *ZCS* ***(b)*** *ZVS*

Figure 2.7: *Soft switching [Images from http://www.lonco-asia.com]*

2.8 Core Material

To improve the coupling of inductive systems, core materials are added to guide the flux and lower the magnetic reluctance. To do so efficienctly, the material must have a relative permeability significantly higher than the permeability of vacuum at the frequency of interest. This happens for two types of materials, ferromagnetics and ferrimagnetics (ferrites). In low frequency applications ferromagnetic cores are common as they have a higher permeability than ferrites in that range. At higher frequencies ferrites are preferred as they have a lower conductivity and consequently lower iron losses.

Manufacturers of ferrites are keen in keeping their core formula a secret. Nevertheless, it is commonly known that most ferrites are predominantly MnZn or NiZn. Owing to its higher initial permeability, MnZn is usually preferred at frequencies under $1\,\text{MHz}$. Above $1\,\text{MHz}$ the permeability drops off rapidly and losses rise steeply, resulting in the usage of NiZn with a lower initial permeability, but higher cutoff ($\approx 10\,\text{MHz}$ to $100\,\text{MHz}$) [8]. The usage of ferrites above $100\,\text{MHz}$ is ill advised as it only induces additional losses and no longer increases the magnetic coupling [9].

Chapter 3

Literature Research

The purpose of this chapter is give an overview of WPT history and recent advances to guide this research. The scope of the literature research remains broad at the beginning and converges to the desired range of efficiencies and powers near the end. It is organized into various sections, starting with a quick summary on history. Secondly, a short investigation into the automotive branch. Thirdly a look on various pad topologies with their advantages and disadvantages. Next, a look on operating frequencies and inverters and lastly a summary about a previous study on the same subject and a company doing something similar.

3.1 History

The American inventor and scientist Nikolai Tesla was the first to study the principles of inductive power transfer. In 1907 he filed a patent for an 'Apparatus for transmitting electrical energy' [10] and consequently became the first to use a tuned transformer to maximize power transfer. The overall efficiency was very low since there were no solid state switches at the time and instead a spark gap was used.

Only around the millenium change, the interest in WPT came back. In 1998 a patent was filed in which at least a single intermediary resonator is placed between the primary and secondary coils to either increase transfer rate or improve alignment accuracy [11]. Kurs *et al.* continued along this path and proposed a system consisting of two loops and two intermediate coils with multiple windings. Additional range and misalignment tolerance are obtained as multiple coupling factors between the resonators increase flexibility. The authors provide a coupled mode theory (CMT) analysis matching reality closely [13]. The overall system transmission efficiency is only 15% for a total efficiency of 40%. In addition, the system did not fulfill the regulations as prescribed by the International Commission on Non-Ionizing Radiation Protection (ICNIRP).

The research above created a new branch in wireless power transfer commonly named resonant inductive power transfer. This branch focuses on loosely coupled resonators with one or more intermediary coils to improve system performance [14, 15, 16, 17]. Modelling was translated to lumped circuit elements and compared with the CMT approach in [14]. The results show both models are accurate for power transfer efficiency calculations. The CMT approach reduces the order of differential equations by half in case the resonators are loosely coupled and have a high quality factor, whereas the circuit model approach is preferred for strongly coupled or low Q resonators for increased accuracy. Conventional research into wireless power transfer without intermediate resonators is also booming.

Jadidian *et al.* have shown that an array of multiple transmitter coils can be used to create a magnetic beam that is much more resilent to lateral and angular misalignment and has a similar efficiency as single coils arrangements at short distances while outperforming traditional technologies at longer distances. However, the control is more complex and the current technology is only focused on low power electronics.

3.2 Pad Design

Extensive research is being conducted on the magnetic resonator of an inductive system. Maximization of power density, power efficiency, transfer distance and misalignment tolerance whilst minimizing leakage flux, weight, cost and volume [19] is key to a proper coupler. Several different architectures are presented, namely circular coils, DD-coils [20], DDQ-coils, bipolar coils, tripolar coils and XPADs. A distinction is made between E and C type structures that have different emissions.

3.3 Inverters

The class D inverter is commonly used thanks to its simplicity, low cost and, low sensitivity to load and coupling varitions. Traditionally, this class of inverters is hard switched yielding lower efficiencies for high frequency WPT. Soft switching is possible, but then the inverter must operated above or below the resonant frequency (depending on the resonant network), inherently decreasing efficiency as well [21]. Koizumi *et al.*, Koizumi *et al.* introduces a solution to the latter problem by adding a series LC tank in series with the load to obtain the same switching conditions as for class E inverters. This increases component count and cost. Typically, this modified circuit is known as class DE inverter [21].

The first resonant converter was introduced in 1975 by Sokal *et al.* The benefit of this design is that it requires only a single switch, reducing complexity even further by removing dead times and the switch output capacitance C_{oss} is used as an inherent part of the topology to obtain ZVS and zero voltage derivative switching (ZVdS). The original designs suffers from an unnecessarily large RF choke inductor to force a DC input current [25] which has significant drawbacks compared to a finite choke. Benefits of a finite feed inductance include [26]:

- reduction in size and cost
- higher load resistance
- possible reduction in required supply voltage
- larger switch parallel capacitor enabling higher frequency of operation
- faster transient response [27]

Aside from the large choke, proper tuned class E inverters incur switch voltage stresses of $3.6V_{in}$. Improper tuning can lead to even higher switch stresss leading to early component failure. Proper tuning of the load network is also necessary to force soft switching. Variations in load resistance and reactance both introduce hard switching. Compared to other resonant inverters, the class E has the lowest power output [28].

Zulinski *et al.* introduced a load-independent class E inverter that is resilient against resistance variations across a wide range. Load independence in this case means a constant output voltage amplitude whilst still mantaining ZVS and ZVdS. The inverter, however, still remains very sensitive to reactance variations in the load network. Design equations for a load independent design for various duty cycles are derived in [30, 31].

Reduced voltage stresses compared to class E are offered by class F. Harmonic frequencies are shorted or effectively open to obtain the desired waveshape. Wide application is low since most practical designs operate at duty cycles higher than 50%, resulting in non-switched mode operation [27]. Another practical drawback is the increased number of tuned elements and the fact that is almost impossible to achieve optimal switching [32, 33].

First introduced by Kee *et al.*, hybrid combinations of class E, class F and class F^{-1} inverters mix the advantages of both topologies. They eventually reach the conclusion that switching is similar to class E, whilst showing a greater tolerance for transistor output capacitance and presenting waveforms of the more desirable class F^{-1}.

All inverters mentioned above are single ended. Their output power can be quadrupled by combining two identical inverters in a push-pull configuration cancelling even harmonics in the process as well [32].

3.4 Megahertz Wireless Power Transfer

With the uprise of wideband semiconductors even higher frequency operation is possible. Currently, several research groups are actively researching WPT in the megahertz range. Among these groups are Stanford and Imperial College London. The most promising frequencies are 6.78 MHz and 13.56 MHz as they are free to use as part of the industrial, scientific and medical (ISM) band. A table depicting the work in the field is shown in table 3.1. One of the earliest ventures in using 6.78 MHz for WPT is [33]. With conventional technology and an EF_2 inverter high efficiencies were already obtained. In [30, 34] he continues his work with improvements in load-independence, an upgrade to GaN, higher power, higher switching frequencies (13.56 MHz) and overall higher efficiencies. The inverter topologies remain class E and class EF_2. Choi *et al.* added intermediary resonators to increase the separation distance to 300 mm. Additionally, they equipped a ϕ_2 inverter to decrease the size of the input choke. Their coils were self wound and therefore EMI could be a serious issue. Also, the inverter is not load-independent. Kwan *et al.*, Kwan *et al.* focuses on wireless charging for e-mobility applications. His early work,[38], on a 100 W charger suffered from a low efficiency. The design already utilizes a load-independent class EF inverter. Rectification is obtained via a class D rectifier. In the follow-up paper, [36], both power and efficiencies are stepped up. The increased power is partly possible by utilizing a class EF inverter in push-pull. The desired voltage on the battery side is achieved with a voltage-tripled class D rectifier. The estimated coupling is only 7%, low compared to other studies. All of the above utilize series resonant networks. In [4] Gu *et al.* show high efficiencies are also possible for parallel matching. Their design focuses on a very high Q resonator structure, which is inherently a parallel network. The design was tested with a phi_2 inverter up to 300 W and with a class D inverter up to 1 kW. The separation distances remain relatively small at just 19 mm and a coupling of 15%.

Year	**Reference**	**Frequency [MHz]**	**Power [W]**	**Efficiency [%]**	**Technology**
2015	Aldhaher *et al.*	6.78 MHz	25	87.2%	Si
2018	Choi *et al.*	13.56 MHz	950	87%	GaN
2018	Aldhaher *et al.*	13.56 MHz	150	90%	GaN
2018	Li *et al.*	6.78 MHz	10	85%	GaN
2018	Surakitbovorn *et al.*	13.56 MHz	300	90.4%	GaN
2019	Aldhaher *et al.*	13.56 MHz	500	-%	GaN
2019	Kwan *et al.*	6.78 MHz	100	65%	GaN
2020	Kwan *et al.*	6.78 MHz	600	84%	GaN
2021	Gu *et al.*	6.78 MHz	1,000	95%	GaN

Table 3.1: *Summary of recent developments in megahertz WPT*

3.5 Power Loss Distribution

In [40, 36] the distribution of losses is visualized. For completeness, both diagrams are shown in figure 3.1. In the leftmost figure, active components sum up to over 50% of total loss, the right is already over 30%. From these it must be concluded that obtaining high efficiencies requires optimization of both active and passive components. New inverter structures are therefore actively investigated [27] to decrease component stresses, costs and increase ZVS range by load independence. Other opportunities lie in the development of very high Q resonators such as [4].

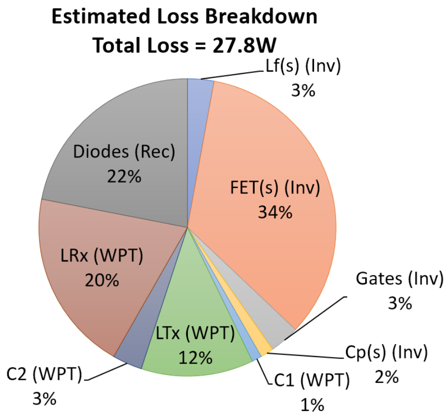

(a) Surakitbovorn et al.

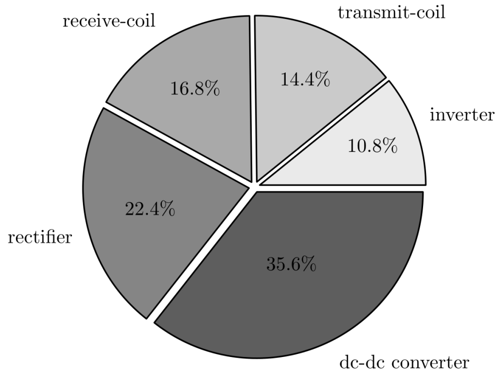

(b) Kwan et al.

Figure 3.1: *Overview of loss distributions for two different WPT systems*

3.6 Regulations

In Europe, there are radio equipment directives and electrical safety regulations to validate whether a device is properly designed. For regulatory approval, the device is tested against ETSI EN 303 417 (Radio) and EN 301 489-1 & -3 (EMC). The first focusses on the effective use of the radio spectrum. Summarized, this defines the permitted range of frequencies, the magnetic field intensity requirements and a series of emission tests. The second set of tests is directed towards interference from the device to its surroundings (emissions) and vice-versa (immunity). Electrical safety regulations are given in standards EN62311 and EN60950-1 or EN62368.

3.7 Standards

In addition to local regulations, the designer can choose to design the system in compliance with one of several standards listed below. In general, they exist to increase interoperability and safety. Organizations like ICNIRP, SAE, IEC and ISO are separate entities not backed directly by companies. Others, like Wireless Power Consortium (WPC) and AirFuel Alliance were established by companies and are competing for a market share.

- ICNIRP, the ICNIRP is at work to investigate possible hazards of non-ionizing radiation (NIR) to the human body. Currently there are two guidelines, one was created in 1998 and the other in 2010. The latter replaces the old guidelines for low frequency time varying electric and magnetic fields (1Hz-100kHz) only.

- SAE J2954/1, society of automotive engineers based standard. Defines three charger classes for EVs rated at 3.7kW, 7.7kW and 11kW. The system is defined around resonant inductive coupling systems that use a frequency of 85kHz and have an efficiency of around 85%. The standard defines methodologies to test the electromagnetic emissions.
- IEC 61980-1:2020, a subset of this standard describes WPT for a range of common voltages. The standard describes the system layout, regulatory boundaries, tests and communication between the car and the (unidirectional) WPT system. Currently, the standard is not ready for bidirectional systems.
- ISO 19363:2020, Addresses safety, transferred power, efficiency, ground clearance and test procedures for unidirectional and static WPT systems. Systems fulfilling these requirements are supposed to be interoperable with IEC 61980 compliant systems.
- AirFuel Resonant, defines a standard to charge several devices simultaneously using inductive resonant coupling alignment free operating at 6.78MHz.
- Qi standard, one of the most used charging standards for handheld devices with inductive coupling and charging powers of up to 30W and operating frequencies between 80-300kHz. Both pads communicate with each other through power modulation.

3.8 Previous Study in Twente

In 2020 another student wrote a thesis on possibilities of WPT and business opportunities [41]. The study itself touched only the surface of the design challenge and is more a global systems engineering document on possible designs. With the business case in mind, the report is a qualitative comparison between several prototypes and lacks a quantitative approach on a technical level. Kalpoe considers the placement of the magnetic structure on the E-bike as constrained by safety, ease-of-use, size, weight, efficiency and cost. The most promising locations are kickstand, a fixture on the front fork or placed similar to the headlight. For data, an FM modulator is placed on the magnetic structure that is orthogonal to the power flux.

Chapter 4

Analysis

The following sections dive deeper into the working principles of resonant inductive power transfer. The first section explains the principles of two basic resonant networks having only a single resonant frequency. Afterwards, a combination of both is introduced and studied. Without losing generality, graphics are provided at 85 kHz. The chapter continues with the introduction of the secondary side to determine the characteristics and find conditions for the optimum coupling efficiency.

4.1 Mono Resonant Circuits

The behavior of series and parallel resonant circuits is investigated in this section. Basic characteristics as gain and input impedance are investigated to form a basic understanding of inductive power transfer (IPT) systems for which the coupling factor equals zero. This is a special case for which there is no power transfer between two coils and the source only sees the resonant circuit.

4.1.1 Series Resonance

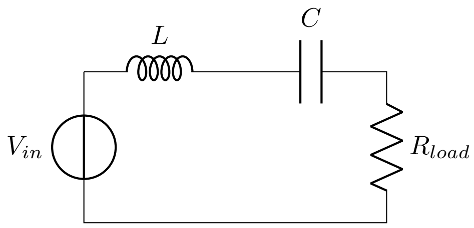

Figure 4.1: *Series resonant circuit with resistive load and voltage source*

In a series resonant circuit (see figure 4.1) a capacitor and inductor form a resonant tank and are in series with the source. Resistive losses are neglected and instead it is assumed that the resonant tank is loaded by a resistive load R_{load}. Assume the source delivers constant voltage and the inductor and capacitor have impedances Z_L and Z_C. The input impedance is derived as in expression 4.1. At frequencies below resonance, the tank impedance is inductive ($90°$ degrees) in nature and the output voltage is always lower than the input voltage. At resonance the tank reactances cancel and the expression reduces to $V_{out} = V_{in}$ (unity gain), such that the entire input voltage is across the load, potentially causing high currents if the load is small with respect to the source voltage. At higher frequencies, the phase angle is inverted to $-90°$ and the output voltage is again lower than the input voltage.

$$Z_{in} = Z_C + Z_L + R_{load} \tag{4.1}$$

Running simulations with $L = 60\,\mu$H and $C = 58.5$ nF (resonance at 85 kHz) for various values of R_{load} yields magnitude and phase plots of the input impedance as in figure 4.2. Clearly, the input impedance has a minimum at resonance. The input current and load power are maximum as a consequence.

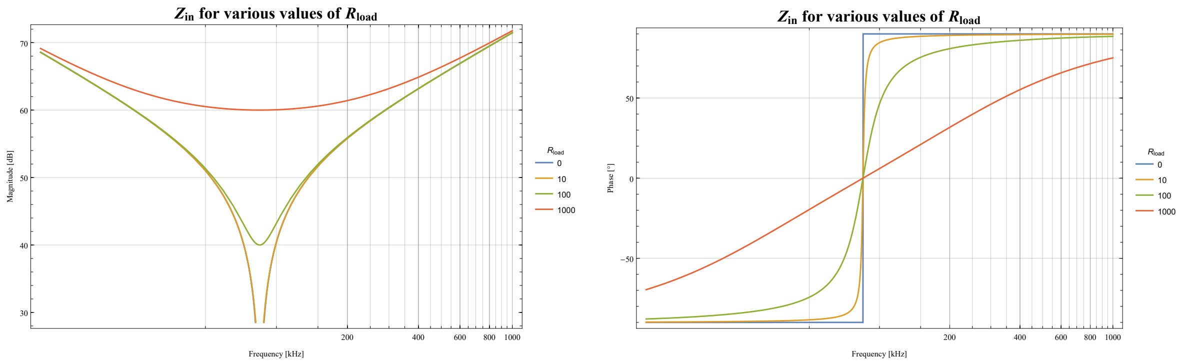

(a) *Magnitude* ***(b)*** *Phase*

Figure 4.2: *Magnitude and phase plot of Z_{in} for a series resonant circuit*

With the experiments in mind, it is also useful to determine the voltage across the primary (V_p). In the following expression, it is assumed that the ESR of the inductor is R_{load}. Hence, the expression including the (native) quality factor (Q) of the inductor is:

$$\frac{V_p}{V_{in}} = Q + 1 \tag{4.2}$$

A consequence of the expression above is that for very high Q inductors, the voltage can easily become excessive causing malfunction due to sparking between the turns.

4.1.2 Parallel Resonance

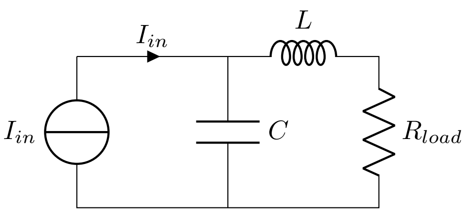

Figure 4.3: *Parallel resonant circuit with resistive load in series with the inductor and input current source*

A parallel resonant circuit is obtained by placing the capacitor, inductor in parallel. The load can be connected in parallel as well, however, IPT systems have the load in series with the inductor. As such, this setup is preferred and depicted in figure 4.3. The input impedance is derived as:

$$Z_{in} = \frac{R_{load} + j\omega L}{1 - \omega^2 LC + j\omega R_{load} C} \tag{4.3}$$

Now, suppose R_{load} is small such that it can be negelected in the expression. The denominator then reduces to $1 - \omega^2 LC$ indicating that the input impedance goes to infinity as the denominator reduces to zero for $\omega_0 = \frac{1}{\sqrt{LC}}$ (natural resonance frequency). Hence values $R_{load} > 0\,\Omega$ limit the maximum input impedance as the denominator does not converge to zero for any frequency. The frequency of maximum impedance (ω_m) in terms of ω_0 and quality factor $Q_L = \frac{\omega L}{R_{load}}$ is then given as in equation 4.4. For $Q_L > 1$, the maximum output impedance is approximated as $|Z_{in,max}| = RQ_L^2$ [42].

$$\omega_m = \omega_0 \sqrt{-\frac{1}{Q_L^2} + \sqrt{1 + \frac{2}{Q_L^2}}} \tag{4.4}$$

This type of circuit is usually driven by a current source since this gives the highest gain and output power. When driving this circuit by a voltage source, it acts as a low pass filter and loses the useful resonance properties.

Similar to the series circuit, simulations with $L = 60\,\mu$H and $C = 58.5\,$nF (resonance at $85\,$kHz) yield the plots as depicted in figure 4.4. Clearly, for these values ω_m stays close to the natural resonance frequency. However, the phase shift is significant and for maximum impedance, you no longer have zero phase shift when R_{load} increases.

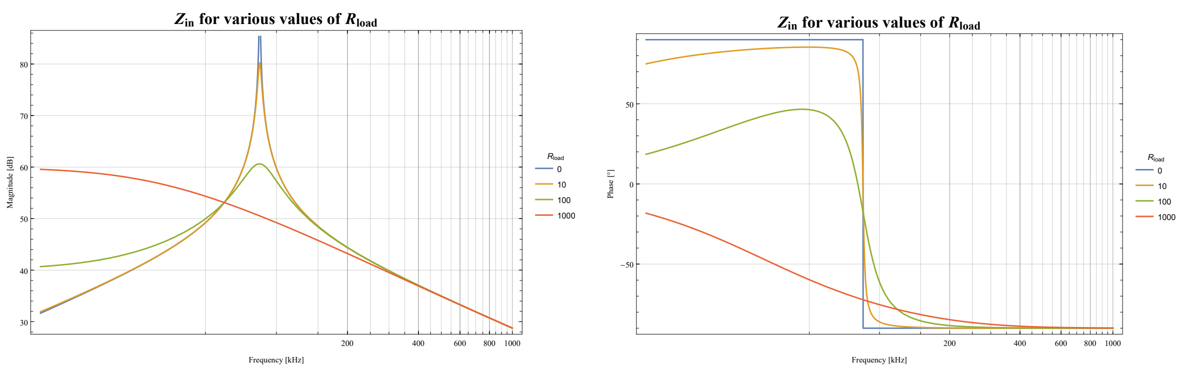

(a) *Magnitude* ***(b)*** *Phase*

Figure 4.4: *Magnitude and phase plot of Z_{in} for a parallel resonant circuit*

4.2 Multi Resonant Circuits

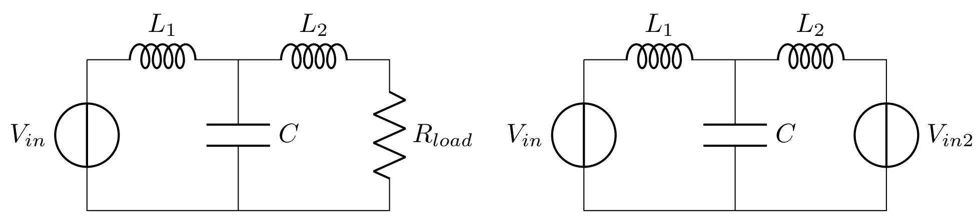

(a) *Resistive LCL circuit* ***(b)*** *Double sided voltage source LCL circuit*

Figure 4.5: *LCL circuit with a resistive load and input voltage source*

Any combination of series and parallel resonant circuits is an hybrid resonant circuit. In this thesis, one particular hybrid circuit is investigated, namely the LCL circuit. Two variants as depicted in figure 4.5 are analyzed below.

4.2.1 Resistive Load

The input impedance of the LCL circuit on the primary side is given in equation 4.5.

$$Z_{in} = \frac{i\omega\left(L_1 + L_2 + i\omega R_L L_1 C - \omega^2 L_1 L_2 C\right) + R_L}{1 - \omega^2 L_2 C + i\omega RC} \tag{4.5}$$

To study the poles and zeros let $R_L \to 0$ to obtain:

$$Z_{in} = \frac{i\omega\left(L_1 + L_2 - \omega^2 L_1 L_2 C\right)}{1 - \omega^2 L_2 C} \tag{4.6}$$

The dynamics are determined by two poles and three zeros. Obviously a zero exists for $\omega_z = 0$. Additionally the expressions for other zeros and poles are given in 4.7 and 4.8 respectively. Clearly the zeros are a function of both inductors and can be tuned separately from the poles by varying L_1. The distance between the poles and zeros is deduced as $\omega_z = \omega_p\sqrt{\frac{L_2}{L_1} + 1}$. Thus for $L_1 \ll L_2$, the zeros diverge to infinity, whereas for $L_1 \gg L_2$ the zeros converge to the same value as the pole. For a symmetrical LCL circuit with $L_1 = L_2$ the zeros are determined to be $\sqrt{2}\omega_p$.

$$\omega_z = \sqrt{\frac{\frac{L_2}{L_1} + 1}{L_2 C}} \tag{4.7}$$

$$\omega_p = \sqrt{\frac{1}{L_2 C}} \tag{4.8}$$

The influence of nonzero R_L is most easily depicted graphically. The resulting graphs are shown in figure 4.6. The load mostly influences the magnitude of Z_{in} at the poles and zeros. It does also influence the resonant frequencies, but this is usually neglected as it is only minor. In contrast with equation 4.8, the poles are dependent on L_2 at resonance. Likewise, the zeros shift as well. The zero in the origin remains.
For both zero and nonzero R_L, the input impedance is inductive at frequencies below ω_p. Between the pole frequency and zero frequencies, the system is strongly capacitive. Above the zero, the system is inductive again.

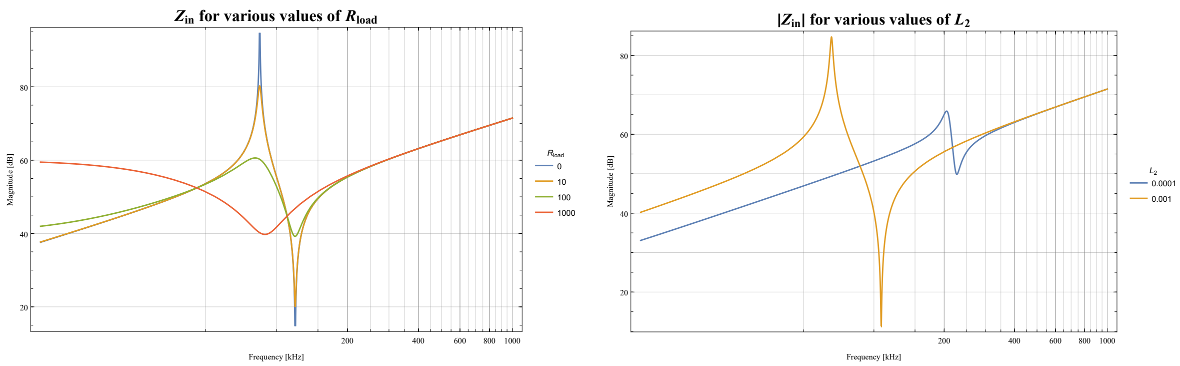

(a) *Sweeping* R_{load} **(b)** *Sweeping* L_2

Figure 4.6: *Magnitude plots of* Z_{in} *for an LCL resonant circuit*

The expression for the load current I_L is 4.9, the graph is given in figure 4.7. Near the pole frequency the terms in the denominator containing R_L sum to zero and the current becomes independent of R_L. The behavior at resonance can therefore be modelled as a current source.

$$I_L = \frac{V_{in}}{-C_1 L_1 \omega^2 R_L - iC_1 L_1 L_2 \omega^3 + iL_1\omega + iL_2\omega + R_L} \tag{4.9}$$

Similar to the parallel and series circuits the inductor voltage is defined as:

$$\frac{V_p}{V_{in}} = \frac{L_2}{L_1} - \frac{i}{Q_1} \tag{4.10}$$

A clear advantage of this structure compared to series compensation, is the unity voltage transfer with zero phase delay for high Q inductors.

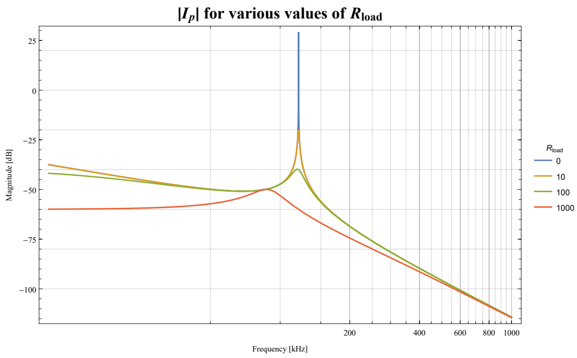

Figure 4.7: *Magnitude plots of Z_{in} for an LCL resonant circuit*

4.2.2 Voltage Source Output

The circuit of figure 4.5 can be characterized based on expression 4.5. The input impedances of source V_{in} is exactly defined by this equation. The input impedance of the other source is found by changing L_1 in the denominator to L_2. As the sources are independent, the principle of superpostion can be applied to find current I_{in} as expressed in 4.11 [43]. For which the input admittances are G_{in}.

$$I_{in} = G_{in}V_{in} + G_{in2}V_{in2} \tag{4.11}$$

The full expressions for the admittances are:

$$G_{11} = \frac{C_1L_2\omega^2 - iC_1\omega R_L - 1}{iC_1L_1L_2\omega^3 + C_1L_1\omega^2R_L - iL_1\omega - iL_2\omega - R_L} \tag{4.12}$$

$$G_{12} = \frac{1}{iC_1L_1L_2\omega^3 + C_1L_1\omega^2R_L - iL_1\omega - iL_2\omega - R_L} \tag{4.13}$$

In case of a fully symmetrical LCL circuit, G_{11} has a clear zero when C_1 and L_2 resonate (see figure 4.8). At this frequency the input current is most dependent on the voltage source V_{in2}, thus marking load independence and current source behavior. Admittance G_{12} adds a phase of $90°$ to the input current. Running the input current at $-90°$ results therefore in a fully real power ouput.

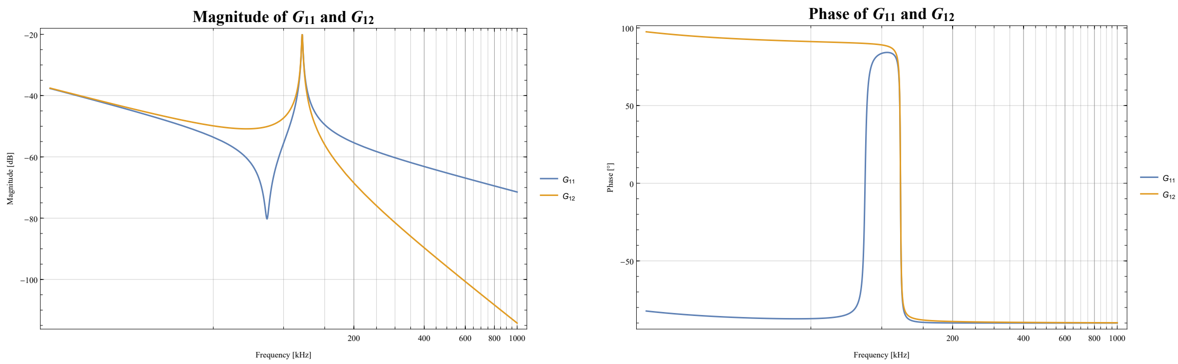

(a) *Magnitude* ***(b)*** *Phase*

Figure 4.8: *Magnitude and phase plots for admittances G_{11} and G_{12}*

4.3 Inductive Power Transfer

The requirement of an IPT system is a coupling between a bare minimum of two inductors. Increased design flexibility and range are obtained when intermediary resonators are introduced [44], but that is not part of this research. Two coupled inductors are modelled as a current controlled voltage source in series with the self inductance of the inductor. The control current is the current flowing through the opposite inductor. The amount of coupling between them is usually expressed as mutual inductance (M_{12}) and is related to the self inductances L_p and L_s and coupling coefficient k_{12}, yielding expression 4.14. The coupling coefficient is a unitless factor defining how much of the generated field traverses through windings of the opposite inductor. As such, it is solely dependent on the orientations and shapes of the inductor pair.

$$k_{12} = \frac{M_{12}}{\sqrt{L_p}\sqrt{L_s}} \tag{4.14}$$

The next sections characterize and compare S-S, LCL-P and LCL-LCL resonant inductive systems. Schematically these systems look like figures 4.9 and 4.10. LCL-P is then a special case of the resonant circuit of LCL-LCL where $L_{S2} = 0\,\text{H}$. All calculations below are carried out according to the following assumptions:

- The system is operating at the resonant frequency $\omega = \omega_0$
- All parasitics are ignored
- The primary and secondary are both tuned to the same resonant frequency
- All elements are linear
- In case of LCL-P or LCL-LCL, the resonance condition is taken to yield a constant current output

The values of components are given as $L_{P1} = L_{P2} = L_{S1} = L_{S2} = 157\,\text{nH}$, $C_P = C_S = 3.5\,\text{nF}$ and $R_L = 60\,\Omega$, $f_0 = 6.78\,\text{MHz}$ and $k_{12} = 0.135$.

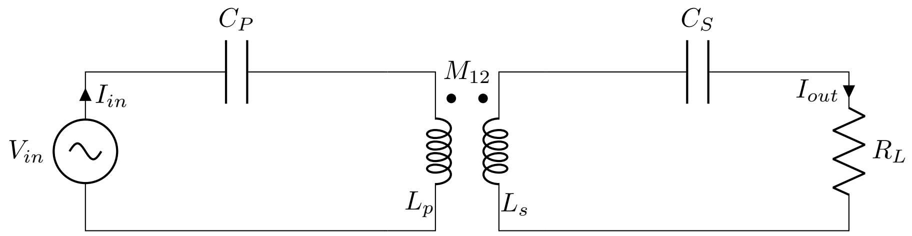

Figure 4.9: *Inductive power transfer S-S resonant circuit*

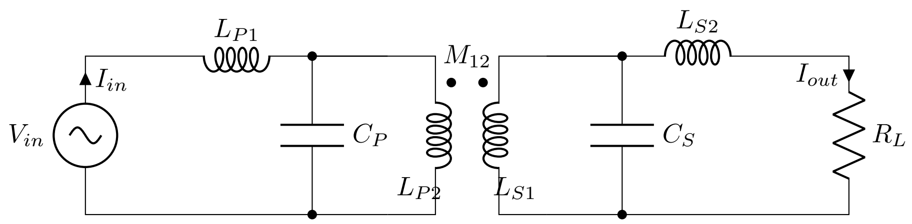

Figure 4.10: *Inductive power transfer LCL-LCL resonant circuit*

4.3.1 Reflected Impedance

The power in the secondary circuit can be modelled at the primary side with a reflected impedance. A general expression is derived based on the circuit in figure 4.9. For all coupled inductors, the reflected impedance is given by expression 4.15 for which Z_S is the secondary input impedance. The reflected impedance as seen by the source is therefore inversely proportional to the equivalent secondary load. It is also quadratic with coupling factor k_{12}.

$$Z_{ref} = \frac{(\omega M_{12})^2}{Z_S} \tag{4.15}$$

The resulting expressions are shown table in 4.1. Noteworthy are the different characteristics at resonance. The series network is purely resistive, the LCL-P network has a capacitive reactance, and the reactance of the LCL-LCL resonant network is dependent on the sizing of the secondary inductors. Setting $L_{S1} = L_{S2}$ removes the imaginary part at resonance, resulting in a fully resistive reflected impedance.

Not every application benefits from the same resonant network. Usually, a higher reflected resistance can be advantageous since it requires less current for similar power transfers, thus minimizing ohmic losses. The magnitude of the reflected impedance is plotted for the above mentioned resonant systems in figure 4.11. The load resistance is important here as the reflected impedance of LCL-P is dominated by its real part for $R_L >> 1\,\Omega$ and shows a reflected impedance similar to LCL-LCL.

	$Z_{ref}\|_{\omega=\omega_0}$
S-S	$\frac{M_{12}^2}{R_L L_S C_S}$
LCL-P	$\frac{M_{12}^2 R_L}{L_S^2} - \frac{M_{12}^2}{L_S\sqrt{L_S C_S}} i$
LCL-LCL	$\frac{M_{12}^2 R_L L_{S2}^2}{L_{S2}^4 + C_S L_{S2} R_L^2 (L_{S1} - L_{S2})^2} - i \frac{M_{12}^2 R_L^2 \sqrt{C_{S1} L_{S2}} (L_{S2} - L_{S1})}{L_{S2}^4 + C_S L_{S2} R_L^2 (L_{S1} - L_{S2})^2}$

Table 4.1: *Expressions for reflected impedances at resonant condition*

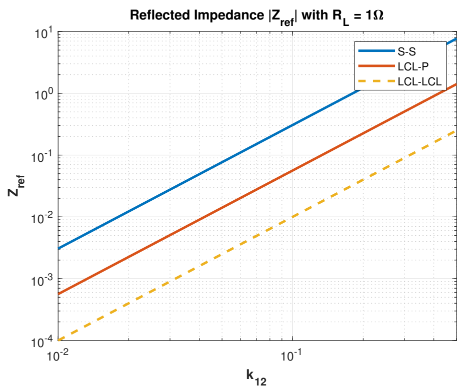

(a) $R_L = 1\,\Omega$

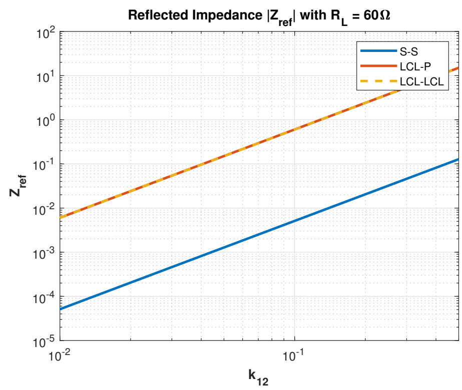

(b) $R_L = 60\,\Omega$

Figure 4.11: *Reflected impedance for* $0.01 < k_{12} < 0.5$

4.3.2 Primary Capacitance

The input power factor is desired to be slightly inductive at resonance for high efficiency and ZVS. To ensure this is the case, the primary capacitance must be sized according to these needs [45]. The desired value of capacitance is found when solving for zero input reactance at the primary side. The expressions for the ideal values of compensation capacitances are defined in table 4.2. Clearly, the expression for P-P is most complicated. This is expected since there is a nonzero complex part in the reflected impedance.

	C_P
S-S	$\frac{1}{\omega_0^2 L_P}$
LCL-P	$\frac{C_{\mathrm{S1}} L_{\mathrm{S1}} \left(k_{12}^4 C_{\mathrm{S1}} R_L^2 - \sqrt{k_{12}^8 C_{\mathrm{S1}}^2 R_L^4 + 2\left(k_{12}^4 - 2k_{12}^2 - 1\right) k_{12}^4 C_{\mathrm{S1}} R_L^2 L_{\mathrm{S1}} + \left(k_{12}^2 - 1\right)^4 L_{\mathrm{S1}}^2} + \left(k_{12}^4 - 4k_{12}^2 + 3\right) L_{\mathrm{S1}} \right)}{2 L_{\mathrm{P2}} \left(k_{12}^4 C_{\mathrm{S1}} R_L^2 + \left(k_{12}^2 - 1\right)^2 L_{\mathrm{S1}} \right)}$
LCL-LCL	$\frac{1}{\omega_0^2 L_{P1}}$

Table 4.2: *Primary capacitor expressions yielding zero input reactance for various compensation networks*

	S-S	**LCL-P**	**LCL-LCL**
I_{in}	$\frac{V_{in} R_L}{M_{12}^2 \omega_0^2}$	$\frac{M_{12}^2 \omega_0 C_{P1} V_{in} (\omega_0 C_{S1} R_L - i)}{L_{P2} L_{S1}}$	$\frac{M_{12}^2 \omega_0^2 C_{P1} C_{S1} V_{in} R_L}{L_{P2} L_{S2}}$
V_{out}	$\frac{i R_L V_{in}}{M_{12} \omega_0}$	$\frac{i M_{12} \omega_0 C_{P1} R_L V_{in}}{L_{S1}}$	$\frac{i M_{12} \omega_0 C_{P1} R_L V_{in}}{L_{S2}}$
I_{out}	$\frac{i V_{in}}{M_{12} \omega_0}$	$\frac{i M_{12} \omega_0 C_{P1} V_{in}}{L_{S1}}$	$\frac{i M_{12} \omega_0 C_{P1} V_{in}}{L_{S2}}$
P_{out}	$\frac{R_L V_{in}^2}{\omega_0^2 M_{12}^2}$	$\frac{M_{12}^2 \omega_0^2 C_{P1}^2 R_L V_{in}^2}{L_{S1}^2}$	$\frac{M_{12}^2 \omega_0^2 C_{P1}^2 V_{in}^2 R_L}{L_{S2}^2}$
Z_{in}	$\frac{M_{12}^2 \omega_0^2}{R_L}$	$\frac{L_{P2} L_{S1}}{\omega_0 M_{12}^2 C_{P1} (\omega_0 C_{S1} R_L - i)}$	$\frac{L_{P2} L_{S2}}{M_{12}^2 \omega_0^2 C_{P1} C_{S1} R_L}$

Table 4.3: *Key equations for various compensation schemes at their resonance conditions*

4.3.3 Output Power

The expression for the output power for different resonant networks is also supplied in table 4.3. The output power for the different resonant networks is plotted in figure 4.12b. Considering the expressions in the table, all output powers are proportional with R_L and quadratic with V_{in}. The difference is an inverse quadratic relationship with coupling and frequency for S-S whilst this is quadratic for LCL-P and LCL-LCL. There is also additional design freedom when choosing LCL-P and LCL-LCL since the primary capacitance as well as an inductance in the secondary determine the output power. Choosing small L_{S2} will result in higher output powers.

4.3.4 Input Impedance

Expressions for the input impedance are supplied in table 4.3. The input impedance plays a key role in the inverter design of following chapters. For this reason the input impedance, is plotted versus coupling for both all resonant networks to indicate the operating range (see figure 4.12a). In the special case when $k \to 0$, the input impedance of the S-S circuit goes to zero, whereas the one for the LCL-LCL circuit goes to infinity. The latter is a favorable safety feature since there will never be a short circuit when the secondary goes out of range. In the case of S-S, the circuit must equip a control system to ensure safe operation within bounds.

4.3.5 Input Current

When comparing the input current between the different resonant networks, it is concluded that only LCL-P has a capacitive reactance. For high R_L the magnitude converges to that of LCL-LCL, similar as what we saw for the input impedance.

4.3.6 Output Current

Concluding from table 4.3, the output current is independent of the load resistance for all resonant networks. The output current is shifted 90^o compared to the input. Similar to what we saw for the other characteristics S-S is inversely proportional to coupling whereas LCL-P and LCL-LCL are proportional to it.

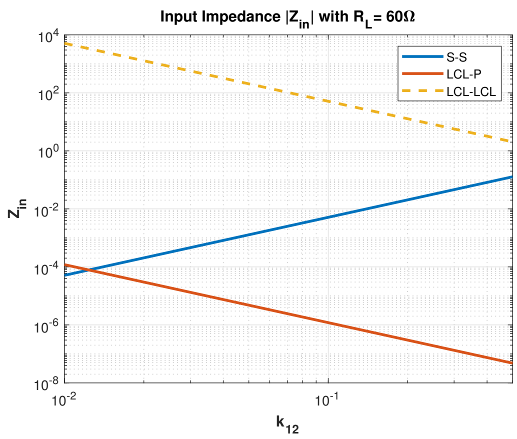

(a) Input impedance for varying coupling

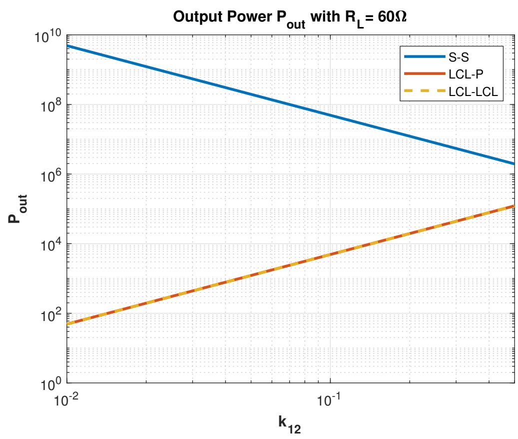

(b) Output power for varying coupling

Figure 4.12: *Input impedance and output power*

4.4 Optimum Coupling Efficiency

The next sections present optimum load resistances and maximum efficiencies for S-S, LCL-P and LCL-LCL. Plots are constructed with the following parameters in mind: $f_{res} = 6.78\,\text{MHz}$, $L_{P1} = L_{P2} = L_{S1} = L_{S2} = 157\,\text{nH}$, $Q_{S1} = Q_{S2} = 100$.

4.4.1 S-S

To consider the coupling efficiency, the rectifier is ignored and the load resistance is directly connected to the AC output as for example in the S-S system in figure 4.9. The losses of the inductors are considered and capacitive losses are ignored. The output power into R_L yields the coupling efficiency as in 4.16.

$$\eta_{transfer} = \frac{P_L}{P_{in}} = \frac{|I_s|^2 R_L}{|I_p|^2 R_p + |I_s|^2 (R_s + R_L)} \tag{4.16}$$

Since there is a dependence on R_L it is desired to know how to maximize the efficiency. The optimum $R_{L,opt}$ is determined by substitution of in and output currents as given in 4.3 and solving for $\frac{\partial \eta}{\partial R_L} = 0$. The result is determined as:

$$R_{L,opt} = \sqrt{\frac{R_s M_{12}^2 \omega^2}{R_p} + R_s^2} \tag{4.17}$$

Generally, this expression is simplified one step further. Substitution of native quality factors $Q_p = \frac{\omega L_p}{R_p}$ and $Q_s = \frac{\omega L_s}{R_s}$ yields:

$$R_{L,opt} = R_s \sqrt{k_{12}^2 Q_p Q_s + 1} \tag{4.18}$$

Substitution of this into 4.16 yields the maximum efficiency in terms of k_{12}, Q_p and Q_s. The product of k_{12} and $Q_p Q_s$ is directly proportional to the efficiency. As such, this relationship is usually used as a figure of merit (FOM) to indicate efficiency. Additionally, it is important to realize that this allows for some flexiblity as coupling can be sacrificed when the quality factors of one or both of the coils is increased or vice-versa.

$$\eta_{max} = \frac{k_{12}^2 Q_p Q_s}{\left(1 + \sqrt{k_{12}^2 Q_p Q_s}\right)^2} \tag{4.19}$$

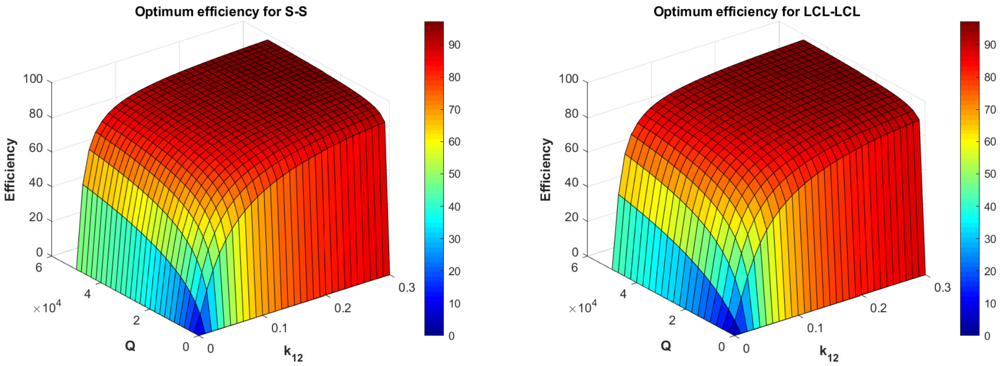

(a) *SS* ***(b)*** *LCL-LCL*

Figure 4.13: *Optimum efficiencies for different resonant networks*

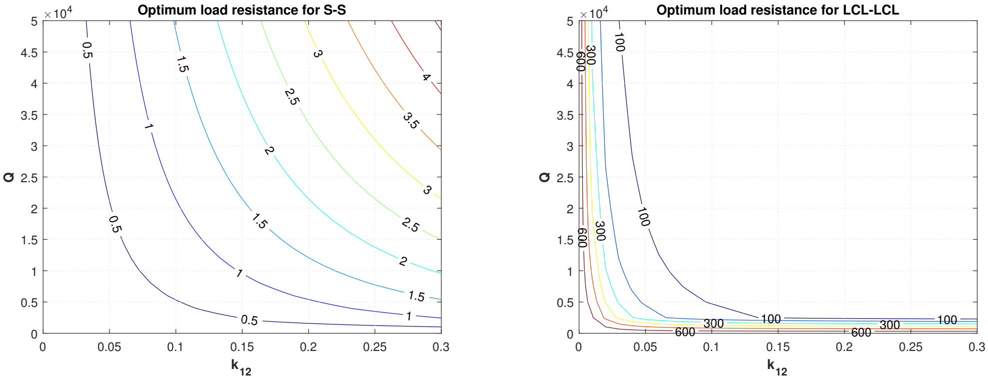

(a) *SS* ***(b)*** *LCL-LCL*

Figure 4.14: *Optimum efficiencies for different resonant networks*

4.4.2 LCL-LCL

Compared to series resonant networks, LCL networks have a higher passive component count and therefore risk a lower efficiency. Similar to S-S, the optimum resistance and maximum efficiencies can be calculated, yielding expressions for optimum LCL-LCL load resistance and efficiency respectively in 4.20 and 4.21. The first term in the denominator of η_{max} is usually not dominant, such that efficiencies similar to S-S are possible. The similarity is visible in the plots from figure 4.13. The optimum efficiency is obtained for very different load resistances as is shown in plots 4.14.

$$R_{L,opt} = \frac{Q_{S2}R_{S2}}{\sqrt{k_{12}^2\omega_0^2C_S^2Q_{P2}Q_{S1}R_{S1}^2 + \omega^2C_S^2R_{S1}^2}} \tag{4.20}$$

$$\eta_{max} = \frac{k_{12}^2Q_{P2}\sqrt{k_{12}^2Q_{P2}Q_{S1}+1}}{2\omega_0C_SR_{S1}\left(\sqrt{k_{12}^2Q_{P2}Q_{S1}+1}+1\right) + k_{12}^2Q_{P2}\left(\sqrt{k_{12}^2Q_{P2}Q_{S1}+1}+2\right)} \tag{4.21}$$

4.4.3 LCL-P

The same procedure was applied to LCL-P to determine the optimum load resistance and maximum efficiency. As it turns out, the optimum load resistance is given by expression 4.22. The expression for the maximum efficiency was derived as well, but is very lengthy and not insightful. Plotting the optimum load resistance and efficiency resulted in the exact same curves as for LCL-LCL. For this reason they are not repeated here.

$$R_{L,opt} = \frac{\sqrt{k_{12}^2 Q_{P2} R_{P2} Q_{S1} R_{S1}^2 + R_{P2} Q_{S1}^2 R_{S1}^2 + R_{P2} R_{S1}^2}}{\sqrt{k_{12}^2 \omega_0^2 C_S^2 Q_{P2} R_{P2} Q_{S1} R_{S1}^2 + \omega^2 C_S^2 R_{P2} R_{S1}^2}} \tag{4.22}$$

4.5 Switching Frequency

The operating frequency is set to 6.78 MHz based on the available ISM frequencies as summarized in table 4.4. Apart from regulation, additional benefits include, smaller component sizes, higher native quality factors due to decreased winding losses, better copper utilization, cost reduction and GaN or SiC switches with better $R_{DS,on}Q_G$ FOM [4]. Also, for LCL-LCL and LCL-P, the power scales quadratically with frequency. Some designs with high power therefore require increased frequencies to achieve the requirements.

Center Frequency	Bandwidth	Availability
6.78 MHz	30 kHz	Locally
13.56 MHz	14 kHz	Worldwide
27.12 MHz	326 kHz	Worldwide

Table 4.4: *Overview of ISM bands applicable to WPT*

4.6 Detuning

An IPT system is in a detuned state when either the primary or secondary resonant frequency or both are unequal to the switching frequency. When this happens, the impedance of the resonator is not resistive but has a reactive part as well. With this in the system, the efficiency drops inherently. The effect of detuning is different between the various compensation networks. With series or parallel networks the influence of detuning results in a single pole or zero moving to another frequency. However, for LCL networks, the additional inductors can be detuned on purpose to have the system behaving slighlty inductive, whilst the resonant frequency of the pad remains equal. A detuned capacitor, however, remains just as bad for all considered networks as all poles and zeros would move. Generally, a detuned system behaves worse due to the added reactive part. Both efficiency and power output are influenced.

In figure 4.15 the real and reactive output powers for several detuned cases of S-S and LCL-LCL are studied. On first glance, both graphs look very similar, however, in case of S-S, the load resistance was lowered to $1\,\Omega$, otherwise the sensitivity of the system was too high. The detuned frequency is related to the resonance frequency as $\omega_{det} = x \cdot \omega_0$, were x is a unitless factor. All cases have either one or two detuned elements at the receiver or transmitter. Near the resonant frequency $x = 1$, there is a large dropoff in output power when the receiver frequency varies either up or down. The influence of transmitter detuning is significantly less, the output power goes up even slightly for frequencies below resonance. It is possible to have both receiver and transmitter detuned, the real output power then goes down in almost all cases. Further effects of detuning are simulated in chapter 7.

4.6.1 Key Takeaways

Concluding this chapter, it is shown that all resonant networks presented here, being S-S, LCL-P and LCL-LCL, have a current source output. The main difference between series and LCL resonant networks is how the frequency and mutual inductance show in the characteristic equations presented in table 4.3. When a series

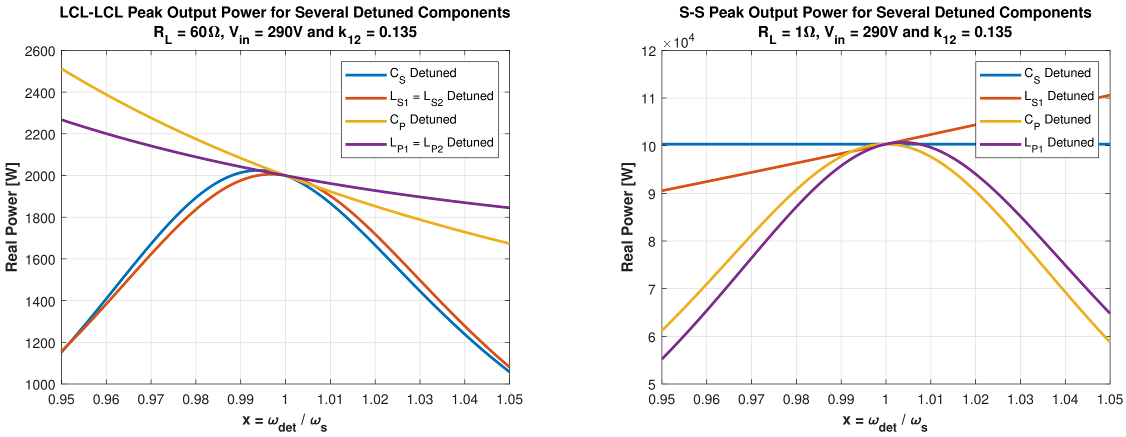

***(a)** LCL-LCL*

***(b)** S-S*

***Figure 4.15:** Output power for several cases of detuning*

characteristic has it in its denominator, the LCL shows it in the nominator and vice versa. This creates opportunities to use both networks, depending on your application. The LCL networks have the highest efficiencies for large loads, whereas the series network has it for low loads. A comparison shows both resonant networks can yield high efficiencies.

Chapter 5

Design of the Inductive Link

The focus of this chapter is on the design of a magnetic resonator. For this work two possible pad designs were modelled of which only one is presented in this chapter. First, the designs were modelled in the FEM tool to obtain a means to quickly iterate through different design variations. An optimum design was chosen after which the FEA results were matched against analytic calculations. The structure of this chapter is similar. All FEM results are obtained with CST Studio Suite 2021. The tool is set to use the magnetoquasistatics solver with tetrahedral mesh and an accuracy of 10^{-6}.

5.1 Considerations

5.1.1 Mechanical Dimensions

Constrained by the requirements, the mechanical outer dimensions must be somewhere around $10\,\mathrm{cm}$x$10\,\mathrm{cm}$.

The minimum cross sectional area of the conductor is defined by the maximum current. The maximum allowable current density is set at $10\,\mathrm{A\,mm^{-2}}$. The previous chapter showed a maximum RMS current of around $50\,\mathrm{A}$. Ideally, the conductor can be etched directly on the PCB, however, this becomes costly for trace thicknesses (t_c) above $60\,\mathrm{\mu m}$ and is therefore not feasible as the trace width (w_c) would become too wide. Standard copper plates have a thickness of $0.5\,\mathrm{mm}$, yielding a trace width of $1\,\mathrm{cm}$.

5.1.2 Pad Shape

The design of a very high efficiency coupler is a design challenge in itself. For this reason, the scope of possible pad design is already limited. On top of this, the maximum allowable dimensions are small, the currents high, available time moderate and misalignment is very probable. On the basis of earlier research a planar square coil offers the best solution. It has the highest misalignment tolerance and offers the best mutual inductance for given parameters [17, 46]. A symmetric transmitter/receiver pair is also beneficial as this offers the highest coupling factor (see figure 5.2a).

5.2 FEM Modelling

5.2.1 Shielding with Ferrite

In WPT systems ferrite shields are added below the antenna to comply with EMI regulations and to improve the coupling between the two pads as was briefly mentioned in chapter 2. There is, however, a limit to the performance benefit. At some point the reluctance of air becomes the dominant factor. To find the relative permeability where this happens, the permeability of the model is swept from 1 to 10,000 to study the effect on

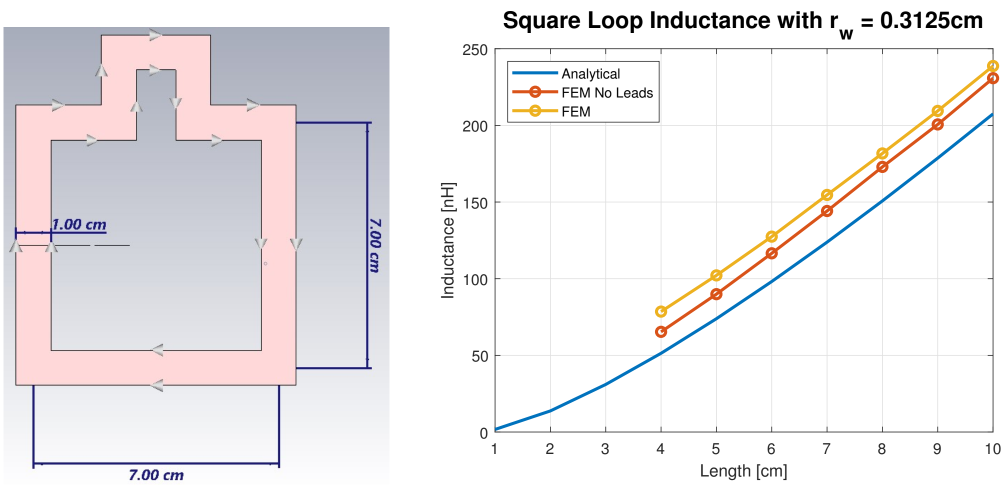

(a) CST 3D Model with leads

(b) Square Loop Inductance

Figure 5.1: *3D model and square loop inductance*

coupling. The resulting coupling coefficients for coils of various sizes are shown in figure 5.2b. It is concluded that increasing the permeability above 100 has little effect on coupling.

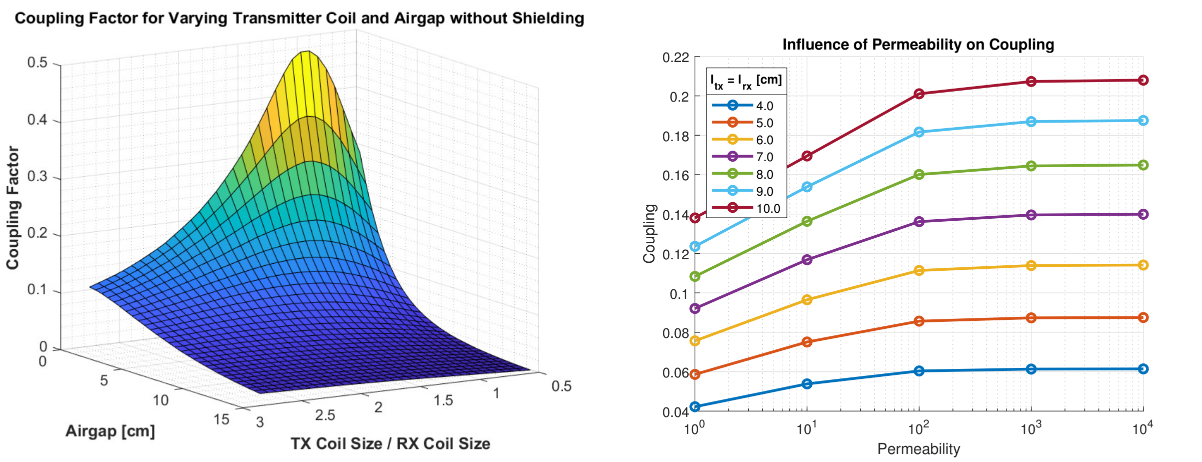

(a) Changing airgap and transmitter/receiver ratio

(b) Results of FEM simulations showing the influence of relative permeability on coupling for nominal airgap separation $5\,\mathrm{cm}$

5.2.2 Number of Turns

The number of turns was swept to determine the relationship with self- and mutual inductance (see figure 5.3). Ultimately, the power constraint required a system with a low self-inductance yielding single turn loops.

5.2.3 Misalignment

As part of the requirements, the system must tolerate misalignments of up to $0.5\,\mathrm{mm}$ and 10^o. The effect of misalignments was studied by parametrically sweeping the orientation of the coils. The variation of the coupling was calculated with respect to the nominal airgap and no ferrite shielding. The results are displayed in figure 5.4. The link is resilient against polar misalignments across all axes and translational misalignments along X and Y with only 3% variation. Changes in the airgap (z-direction) show a higher variation in the negative direction compared to the positive.

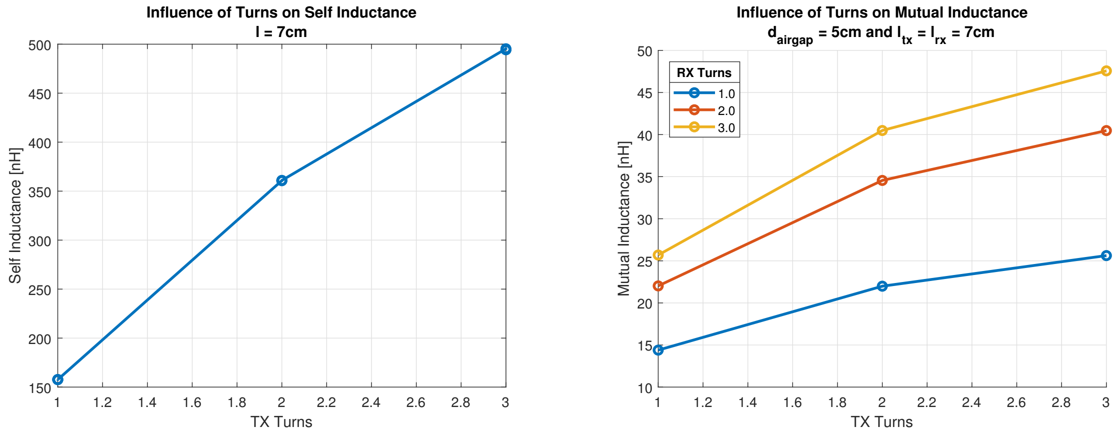

(a) *CST 3D Model* **(b)** *Square Loop Inductance*

Figure 5.3: *FEM Simulations Results showing the influence of the number of turns on the self- and mutual inductance*

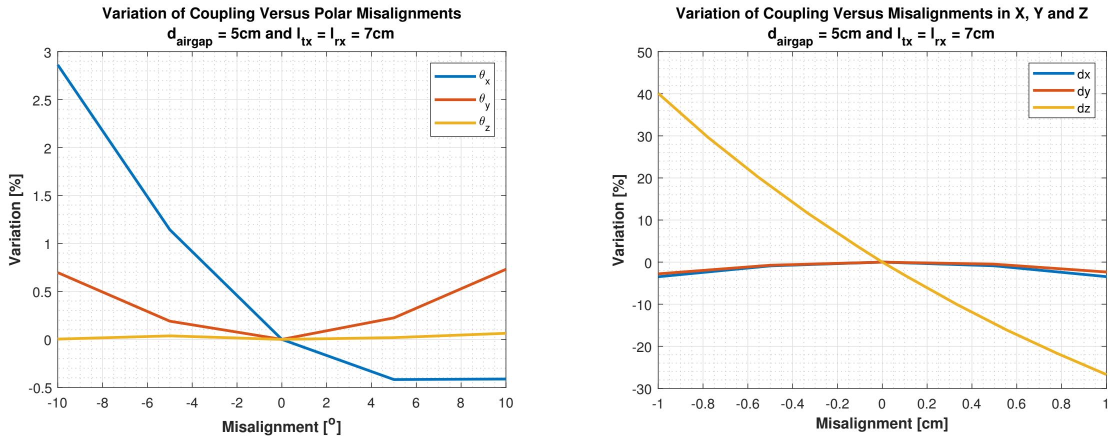

(a) *Polar* **(b)** *X,Y and Z*

Figure 5.4: *Variation of coupling factor for polar and lateral misalignments*

5.3 Analytic Calculations

5.3.1 Self Inductance

The bottom line for analytic analysis is the simplicity of the magnetic structure. Analytic expressions for simple designs, such as planar loops, can reach high accuracies by using the law of Biot-Savart. This law relates a current to the magnetic field at radius r. The full expression is supplied in expression 5.1. To find the inductance, the magnetic field on any point inside the loop bounded by the current must be calculated. A surface integral over the field intensity yields the flux ϕ. The inductance is then determined as ϕ/I.

The square magnetic loop antenna is one of such simple architectures and can be analytically calculated by the procedure above. In [47, 48], exactly this is done to find expression 5.2. Implicitly it is assumed the conductors have a circular cross section. Although the accuracy will decrease with this assumption, it still offers useful insight whether the simulation results are trustworthy at all. Doing the calculations with the parameters as per table 5.1, the inductance is found to be $137\,\mathrm{nH}$, lower than the one from FEM. The deviation between FEM and hand-calculations is approximately 15%.

$$B(r) = \frac{\mu_0 I}{4\pi} \int \frac{\mathrm{d}\mathbf{l} \times \mathbf{r}}{|\mathbf{r}|^3} \tag{5.1}$$

$$\begin{aligned} L_{sl} = \frac{2\mu_0}{\pi} \Bigg[& (l - r_w) \sinh^{-1} \frac{l - r_w}{r_w} - l \ln\left(1 + \sqrt{2}\right) + l\sqrt{2} \\ & + r_w \sinh^{-1} \frac{r_w}{l - r_w} - 2\sqrt{(l - r_w)^2 + r_w^2} \Bigg] \end{aligned} \tag{5.2}$$

5.3.2 AC Resistance

The FEM software does not calculate the AC resistance. In high frequency applications the AC resistance is substantially higher than the DC resistance due to the skin- and proximity effects. The latter effect is assumed negligible since the pads have a single winding only. However, there will be an end-winding effect that can cause the AC resistance to be higher, especially for big currents. To determine the AC resistance, first the DC resistance is estimated after which it is multiplied by a the skin-ratio. The skin-ratio, F_{skin}, is the ratio between DC and AC resistance based on the skin-effect. The DC resistance is estimated based on the conductor length, cross sectional area and resistivity of copper. With a conductor width of $w_c = 1\,\mathrm{cm}$, thickness of $t_c = 0.5\,\mathrm{mm}$, conductor length (including end windings) of $L_c = 29\,\mathrm{cm}$, resistivity of copper $\rho_{copper} = 1.68 \cdot 10^{-8} \Omega m$.

$$R_{DC} = \frac{\rho_{copper} L_c}{w_c l_c} = 97.0 \mu\Omega \tag{5.3}$$

The skin-ratio is determined as [49]:

$$F_{skin} = \frac{1}{2} \frac{t_c}{\delta} \frac{\sinh\left(\frac{t_c}{\delta}\right) + \sin\left(\frac{t_c}{\delta}\right)}{\cosh\left(\frac{t_c}{\delta}\right) + \cos\left(\frac{t_c}{\delta}\right)} \tag{5.4}$$

with δ the skin-depth defined as:

$$\delta = \frac{\rho_{copper}}{\sqrt{\pi \mu_0 f}} \tag{5.5}$$

At the frequency of operation $\delta = 25.0\,\mu\mathrm{m}$ thus F_{skin} evaluates to 99.9, R_{AC} evaluates to $9.72\,\mathrm{m}\Omega$.

5.3.3 Key Takeaways

As an overview of this chapter, table 5.1 is constructed. These results are compared to experiments in chapter 9.

Airgap	$5\,\mathrm{cm}$	**Loop Length**	$7\,\mathrm{cm}$
Loop Width	$7\,\mathrm{cm}$	**Conductor Width**	$1\,\mathrm{cm}$
Conductor Thickness	$5\,\mathrm{mm}$	**Turns**	1
DC Resistance	$97\,\mu\Omega$	**AC Resistance**	$9.7\,\mathrm{m}\Omega$
Analytic Self-Inductance	$137\,\mathrm{nH}$	**FEM Self-Inductance**	$157\,\mathrm{nH}$
FEM Coupling	0.135		

Table 5.1: *Nominal pad design parameters and results*

Chapter 6

System Design

The purpose of this chapter is to introduce the reader to the practical implementation of the WPT system. The high-level implementation of any WPT system is generally very similar and looks like figure 6.1. The various blocks are explained within this chapter starting with a choice of resonant network. This is followed by sections describing the load and the rectifier. Then a thorough derivation of the load-independent class E inverter along with its design equations is presented. The very last section lists the actual implementation details of the practical system.

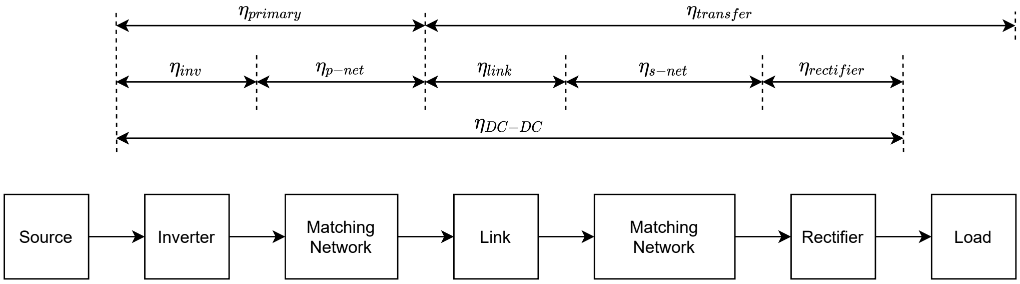

Figure 6.1: *System overview with indicated subsystem efficiencies*

6.1 Resonant Network

The LCL network in both primary and secondary was selected. This choice was made based on the following advantages compared to S-S.

- The primary is at all times safe against short circuits, even when the secondary decouples
- The resonator voltages would remain relatively low, at maximum $3.6V_{in}$. This also benefits the resonant tanks as less voltage stresses are applied, hence requiring less capacitors in series
- The LCL-resonant network is better suited to serve as load for the load-independent class E inverter because
  - A low-inductive pad creates a high input impedance
  - In contrast with S-S, the input impedance for LCL-LCL increases for lower coupling factor, hence the inverter would remain ZVS switched at all times
- There is also some novelty in trying this as the author could not find anyone else doing this

The main drawbacks are increased number of components, hence potentially higher loss and a difficulty in obtaining high output power.

6.2 Load

Eventually, the power must be transferred to a load, a battery. A standard value for the load resistance is found by estimating typical e-bike battery pack. The selected model is the Bosch Powerpack Performance 500. This is a 40 cell pack configured as 10s-4p consisting of cylindrical lithium-ion cells. The Sony VTC6 is picked as high performance cylindrical cell. A CC-CV charge profile for this cell is shown in figure 6.2. During CC the equivalent resistance changes from $2.8\,\Omega$ to $4.2\,\Omega$. The CV charge portion is required to fully utilize the offered capacity. During this, the resistance changes significantly, from $4.2\,\Omega$ to $42\,\Omega$. The equivalent resistive DC load, $R_{L,DC}$, for the entire battery pack thus ranges from $7\,\Omega$ to $420\,\Omega$ for a full charging cycle. For simplicity the load in simulations and experiments will be set to $60\,\Omega$. This will be used as reference point for maximum power transfer. This value presents a proper tradeoff between a low-inductance resonator and high output power. CC-CV charging cycles will not be implemented in this thesis.

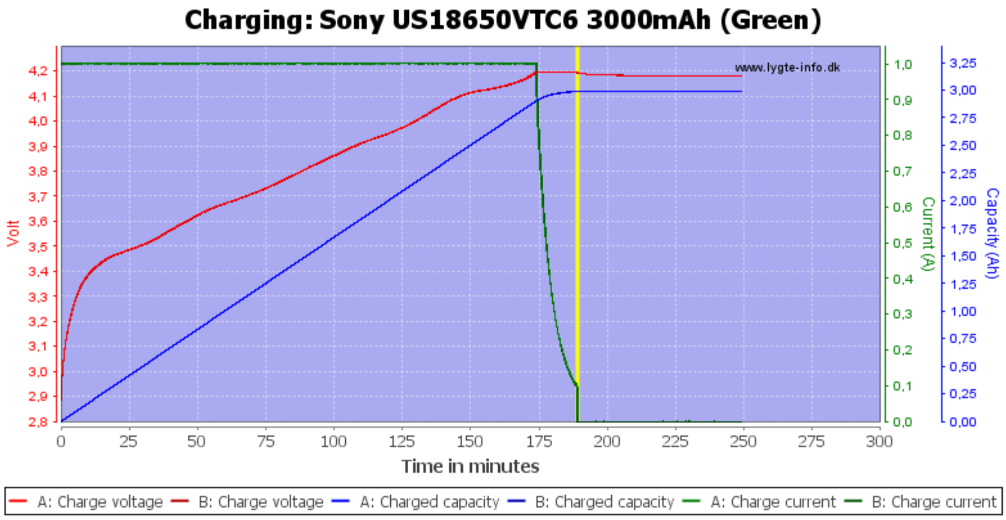

Figure 6.2: *Sony VTC6 charging curve. Charging procedure CC-CV.*

6.3 Current Driven Rectifier

The power transmitted to the receiver must first be rectified before it can store energy in a battery system. A passive full bridge rectifier with a low pass load network is used to do this. The load network consists of a filter capacitor to suppress harmonic content, and a resistor, absorbing real power.

The appropriate value for the filter capacitor is important to minimize ripple. The load network shows a low-pass characteristic conform expression 6.1. The second harmonic is dominant due to rectification. A minimum viable filter capacitor therefore aims towards a -3dB point well below the second harmonic. The minimum capacitor value is therefore: $C_{filter,min} > \frac{1}{\omega_2 R_L}$, with ω_2 as the second harmonic frequency.

$$Z_{eq} = \frac{R_L}{1 + j\omega C_{filter} R_L} \tag{6.1}$$

The input impedance of a current-driven rectifier is calculated assuming steady state and a first harmonic approximation. Given the circuit in figure 6.3, the source current is expressed as $i_{in}(t) = I_{in}\sin(\omega t)$. The capacitor C_F averages the input current resulting in an output current of $I_{out} = 2/\pi I_{in}$. The rectifier input RMS current can therefore be calculated by substitution of the two to be $I_{rms,in} = \pi/(2\sqrt{2})I_{out}$. The output voltage is kept steady due to the capacitor, resulting in an square wave input voltage with a fundamental peak voltage of $V_{p0} = 4/\pi V_{out}$. Rewriting this to the rectifier RMS input voltage yields $V_{rms,in} = (2\sqrt{2})/\pi V_{out}$. The rectifier input impedance is then obtained as per expression 6.2 [50].

$$\begin{aligned} R_{AC} &= \frac{V_{rms,in}}{I_{rms,in}} \\ &= \frac{8}{\pi^2} R_L \end{aligned} \tag{6.2}$$

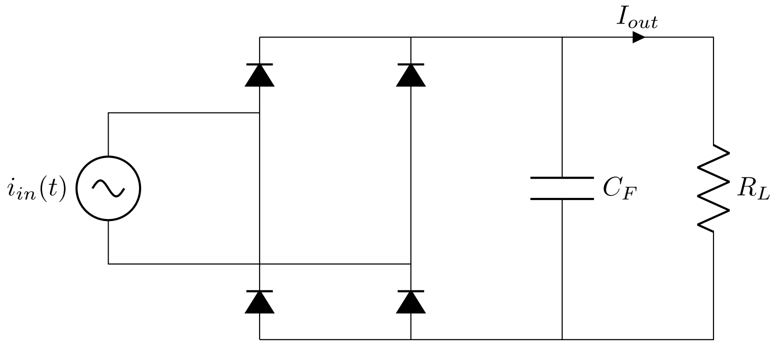

Figure 6.3: *Current driven full bridge rectifier circuit diagram*

6.3.1 Rectifier Parasitics

Ideally, the rectifier acts as an impedance transformer to scale the load resistance. In practical systems this is never achieved because of the shunt capacitance of diodes, creating a slightly capacitive input impedance. A small choke inductor cancels these effects largely.

6.4 Class E Inverter

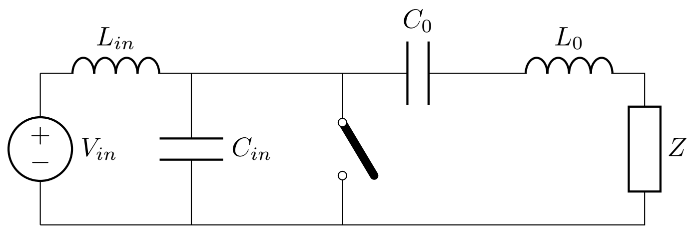

Figure 6.4: *Generic class E inverter circuit diagram*

The class E inverter is a class of resonant converters in which a resonant tank circuit is inserted to improve the efficiency. The resonant tank is added for harmonic suppression. The input inductor has a high reactance at the switching frequency to give a DC like input current and is often assumed infinite to simplify analysis. The choke ultimately limits the transient response to changes in the operating point and is considered slow compared to for example the ϕ-inverters. The shunt capacitor across the switch is added to accommodate ZVS and ZVdS. Depending on the switch the parasitic capacitance is adequate, or a separate capacitor is added. Although highly efficient, a direct disadvantage is the high peak switch voltage ultimately leading to the lowest output power compared to other resonant inverters [28].

6.4.1 Mathematical Derivation

Load-independent class E inverter operation is key in the design of the demonstrator. Load-independency ensures the inverter stays within the ZVS region for efficient switching opertation. The amplifier is designed in line with work by Zhang. His work focuses on a readable and intuitive model to understand the design parameters. He does so by introducing a Thévenin model to calculate the solution. The derivation is partially embedded in this work, however, for a full step-by-step derivation consult [31]. Some of the lengthy expressions are supplied in appendix C.

The class E-inverter circuit is characterized by a switch, two inductors and two capacitors (see figure 6.4). The solution is derived for a duty cycle of $D = 0.5$. Between $0 \leq t \leq \frac{1}{2}T_s$, the switch is open and the switch is closed for $\frac{1}{2}T_s \leq t \leq T_s$. To find a solution, it is necessary to define assumptions, initial and boundary conditions, and lastly some definitions. The definitions make the mathematical expressions easier to read and interpret. All are defined below, starting with the assumptions:

- The components are linear
- The circuit components do not have parasitic impedances
- The bandpass filter formed by L_0 and C_0 is assumed to have a high quality factor resulting in a sinusoidal output current: $i_o = I_0 \sin(\omega_s t + \theta)$. With θ as the phase angle between the falling edge of v_{gs} and the rising zero crossing of the output current (see figure 6.5b).
- The circuit is operating in steady state
- The circuit is operating in the ZVS and ZVdS region

The boundary and initial conditions are:

- The initial input current is: $i_{in}(t = 0^-) = I_{in}$
- The initial condition across the input inductor is: $V_{in} - v_{ds}(t = 0^-) = L_{in}\frac{di_{in}(t=0^-)}{dt}$.
- The first boundary condition is a consequence of ZVS: $v_{ds}(t = 0.5T_s) = 0V$
- The second boundary condition is a consequence of ZVdS: $i_{C_{in}}(t = 0.5T_s) = 0A$.

Lastly, the definitions are:

- The switching frequency is ω_s
- The input resonant frequency of the LC input circuit is ω_{in}
- The ratio between the input resonant frequency and switching frequency is: $q = \frac{\omega_{in}}{\omega_s}$
- Set $Z_{in} = \sqrt{\frac{L_{in}}{C_{in}}}$ (not the input impedance)

The goal is to solve the circuit when the switch is open. Together with the assumptions, this yields the simplified circuit model in figure 6.5a. Writing down Kirchoff's current law yields:

$$i_{in} = i_{C_{in}} + i_o \tag{6.3}$$

Substitution of first order differential equations for the capacitor and inductor yields:

$$L_{in}C_{in}\frac{d^2 i_{in}}{dt^2} + i_{in} = I_o \sin(\omega_s t + \theta) \tag{6.4}$$

With the initial conditions above, it is possible to find a solution to this differential equation for $i_{in}(t)$:

$$i_{in}(t) = \frac{V_{in}}{Z_{in}}\sin(q\omega_s t) + I_{ini}\cos(q\omega_s t) + I_o\frac{q}{q^2-1}\sin(\omega_s t + \theta) - I_o q\frac{q\cos(q\omega_s t)\sin(\theta) + \sin(q\omega_s t)\cos(\theta)}{q^2-1} \tag{6.5}$$

The only remaining unknown is I_{ini}. To remove this from the expression, it is noted the change in current during on and off states must be the same:

$$i_{in}(0) - i_{in}(\frac{1}{2}T_s) = \frac{V_{in}}{L_{in}} \frac{\pi}{\omega_s} \tag{6.6}$$

Solving this once again, one finds an expression for I_{ini} (see appendix C) that can be back-substituted into the earlier expression for $i_{in}(t)$. Similarly it is possible to derive expressions for $i_{C_{in}}$ and v_{ds} for $0 \leq t \leq \frac{1}{2}T_s$
Solving the expression of v_{ds} for the boundary condition of ZVS one finds:

$$V_{in}\left[2 + \frac{q\pi}{\tan\left(\frac{q\pi}{2}\right)}\right] + \frac{2q^2}{1-q^2}\frac{\sin(q\pi)\sin(\theta)}{2\sin^2\left(\frac{q\pi}{2}\right)}Z_{in}I_o = 0 \tag{6.7}$$

The effect of the load on ZVS is captured in the second term with I_o. To create a load-independent inverter, the output current must be removed from the constraint. Clearly, the second term must go to zero, with the earlier $\theta = \theta_{ZVS} = 0^o$ the expression can be solved and yields $q = 1.2915$. A consequence of this is that the ZVS range is also independent of Z_{in} when $\theta = \theta_{ZVS}$.
Similarly, a necessary condition can be calculated to achieve ZVdS. Additionally, this will also be a boundary condition for ZVS since $\frac{dv_{ds}(\frac{1}{2}T_s)}{dt}$ in a practical system must always be smaller than zero due to the third quadrant operation. By solving $i_{C_{in}}$ for the applicable boundary condition results in $V_{in} = 0.47I_oZ_{in}$. To determine the output voltage amplitude under ZVS conditions:

$$V_o = \frac{2}{T_s}\int_{T_s} v_{ds}(t)\sin(\omega t + \theta)dt \tag{6.8}$$

This is found to be $V_o = 1.59V_{in}$. Combining this with the earlier expression for V_{in} we find $\frac{Z_{in}}{R_o} = 1.33$. Hence for this ratio, the system is operating with ZVS as well as ZVdS. From the earlier conclusion that the condition of ZVS is independent of Z_{in} as well as operation in third quadrant, a necessary condition for ZVS becomes:

$$Z_{in} \leq 1.33R_{o,min} \tag{6.9}$$

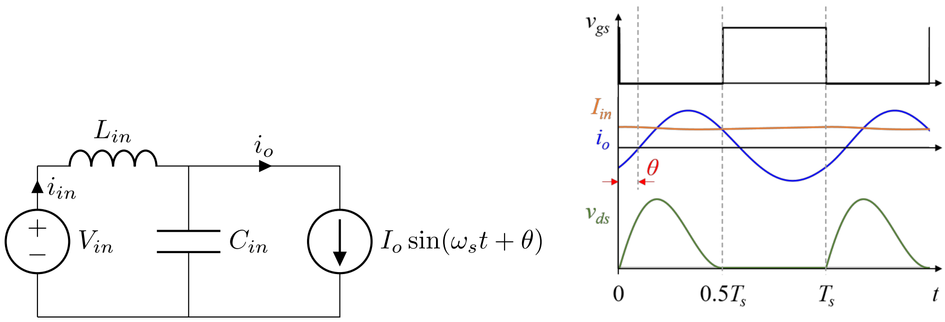

***(a)** Simplified class E circuit model in off state*

***(b)** Class E waveforms [31]*

***Figure 6.5:** Class E simplified calculation model with waveshapes*

6.5 Component Values

The switching device is picked as the GS66508B, the SiC diode in the rectifier is the STPSC406D. Earlier research has shown both are top of the line products currently available [51]. The breakdown of this switch is at $650\,\text{V}$, directly limiting the maximum input voltage to $180\,\text{V}$ $(650/3.6)$. Incorporating a safety margin, the maximum input voltage is set at maximum $V_{in,max} = 150\,\text{V}$. With the desired output power at $1\,\text{kW}$ and the standard harmonic suppression factor of 12 introduced by [31], it was impossible to create the bandpass filter. As such, the harmonic suppression factor was lowered to 3 (see equation 6.15). The desired component values were found via the equations 6.10 - 6.19.

$$V_o = 1.59V_{in} \tag{6.10}$$

$$I_{o,max} = \frac{2P_{o,max}}{V_o} \tag{6.11}$$

$$q = \frac{\omega_{in}}{\omega_{res}} = 1.2915 \tag{6.12}$$

$$\frac{Z_{in,max}}{R_L} \leq 1.33 \tag{6.13}$$

$$\frac{X_{o1}}{Z_{in,max}} = 0.21 \tag{6.14}$$

$$X_{o2} = \frac{3V_o}{I_{o,max}} \tag{6.15}$$

$$L_{in,max} = \frac{Z_{in,max}}{q\omega_s} \tag{6.16}$$

$$C_{in} = \frac{1}{(q\omega_s)^2 L_{in}} \tag{6.17}$$

$$C_0 = \frac{-0.75}{\omega_s} \frac{1}{X_{o1} - 0.5X_{o2}} \tag{6.18}$$

$$L_0 = \frac{X_{o2}}{2\omega_s} \frac{1}{4\omega_s^2 C_0} \tag{6.19}$$

With R_L at $60\,\Omega$ and $k = 0.135$, the desired antenna inductance for LCL-LCL can be calculated according to table 4.3 as well as the desired resonant network capacitances. As a check the definition for $R_{L,opt}$ is used to verify whether the resulting system has a sufficient link efficiency. Both input- and bandpass inductor were self wound according to appendix A.

Chapter 7

Simulations

Before the actual PCB was designed, the entire system was simulated in LTSpice. The simulations were built up in steps, starting with ideal components to verify whether it was at all possible. The full system was simulated in three separate steps. First, the LCL-LCL resonant network tested against the analytical expressions in chapter 4. The input impedance as well as the output power was studied under various circumstances. The second model consisted of the class E load-independent inverter of chapter 6. Similar tests were performed to validate the ideal model performance as well as detuning the system. The last model is a full system model combining the two models above, with the rectifier added to the secondary plus as many models from component manufacturers as possible. The model files are found in appendix B, the models are discussed in the same order as above.

7.1 LCL-LCL

The purpose of this simulation was to verify the findings of chapter 4 and study the effect of detuning on the input impedance. In figure 7.1 several bode plots are shown for two different couplings. For $k = 0.05$, the behavior is similar as in the analysis. However, for $k = 0.135$ the pole at $6.78\,$MHz splits into several sub frequencies. In S-S compensated circuits, this phenomenon is known as frequency splitting (bifurcation) and is a consequence of the system getting overcoupled [52, 15]. As a consequence, maximum output power is obtained to the pole left from the original resonant point. However, no such problems were encountered in this case, the output power remained exactly $1\,$kW. The input impedance was calculated for $k = 0.135$ to be $38.4\,\Omega$. The ripple current amplitude in the pad is $45\,$A.

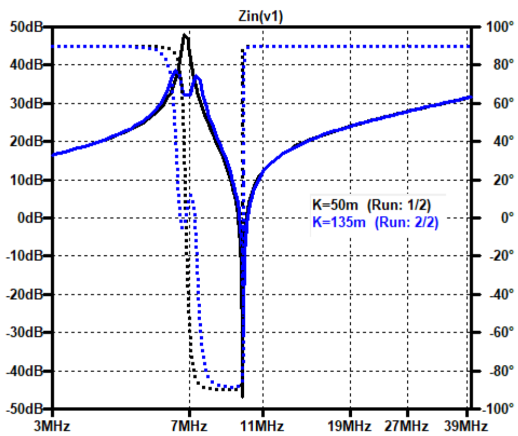

Figure 7.1: *Bode plots for the input impedance tuned system with coupling $k = 0.05$ and $k = 0.135$*

The importance of a tuned system is highlighted when simulations are ran for only a few detuned cases. Suppose the capacitor of the primary has a tolerance of 5%. If this results in the primary capacitance being 5%

lower, the resulting input impedance will have a 14.0^o inductive phase and a 12% drop in output power. A 5% higher value will result in a -19.5^o capacitive phase, but the output power will increase by 20%.

Detuning the secondary has an even worse effect on the performance. With the secondary capacitance at 95% of the desired value, the input phase angle becomes capacitive at -23.7^o and the output power drops with 30%. Increasing the capacitor by 5% yields an inductive phase but the output power still drops to 95% of the designed value with an 21.8^o inductive phase.

When only considering little change in capacitance the system performance detorates. Considering all other possible component tolerances it must be clear that the system must be build with low tolerance components.

7.2 Class E Inverter

The ideal load-independent class E inverter model as supplied in the appendix is fully customizable. The timestep must be low, otherwise the results are inaccurate and the v_{ds} waveform would look asif the inverter was not in the ZVS region. Additionally, the model suffers from minor inaccuracties due to rounding errors in the component values.

The model was verified for $P_{o,max} = 1.2$ kW and $V_{in} = 150$ V. The suppression of the harmonic was set to 12 to verify the findings of [31]. A full list of derived component values is supplied in table 7.1. In figure 7.2a the drain-source waveforms are given when stepwise sweeping the load resistance from the minimum value $R_{out,min}$ to $100\,\Omega$ and 1 kΩ. For the first two, the drain-source voltage slightly undershoots the desired turnoff point. This is caused by the rounding errors mentioned previously. Other conclusions from the figure are that clearly the design is going for a ZVdS turnoff when the load resistance is $R_{out,min}$. For the other steps, the design is solely operating in the ZVS region. The peak amplitudes of v_{ds} are also different, where the lowest load-resistance incurs the highest voltage stress. Suppression of the second harmonic in the output current was investigated in figure 7.2b. The second harmonic content is approximately suppressed by a factor 24. For $R_{out,min}$ the input averages 8 A with a 11 A ripple amplitude. The output has a 7 A RMS value and therefore shows 20 V peak-peak. The power output is exactly 1.2 kW for $R_{out,min}$ and drops for a higher load-resistance as expected.

V_{in}	150 V	$P_{o,max}$	1200 W
$R_{outmint}$	$23.7\,\Omega$	$Z_{in,max}$	$31.52\,\Omega$
$I_{o1,max}$	10.06 A	V_o	238.5 V
X_{o1}	$6.62\,\Omega$	X_{o2}	$284.4\,\Omega$
L_{in}	572.9 nH	C_{in}	576.6 pF
L_0	1.060 µH	C_0	608.5 pF

Table 7.1: *Parameter values for a class E inverter*

A variation of 5% in L_0 already causes the system to enter hard-switching for $R_{out,min}$. The non-zero reactance of the load network causes Z_{in} to change and therefore also influences the ZVS and ZVdS conditions. The effect of varying L_0 decreases for increased load resistances.

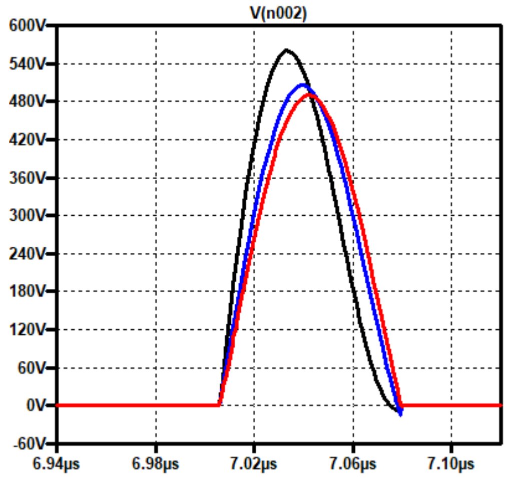

(a) v_{ds} for different load resistances $23.7\,\Omega$ (black), $100\,\Omega$ (blue) and $1\,\mathrm{k}\Omega$ (red)

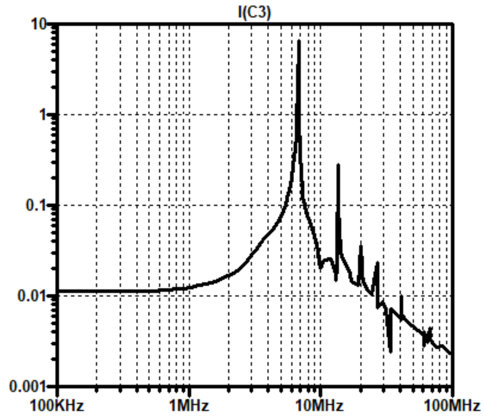

(b) FFT plot for the output current

Figure 7.2: *v_{ds} and i_o*

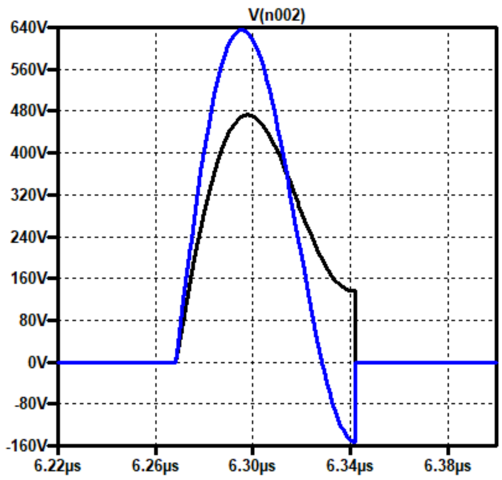

Figure 7.3: *Detuned v_{ds} waveforms for 95% and 105% ideal L_0 (respectively black and blue)*

7.3 Full System

Combining the models above with results from the impedance analyzer as well as libraries provided by the manufacturers shows three possible problems:

- Ringing as a result of cascading a series bandpass filter with a parallel LC circuit. This would show as amplitude modulation in for example the drain-source voltage (see figure 7.4a). Caution is advised as the ringing can cause v_{ds} to rise above the maximum specified breakdown voltage.
- The non-linear output capacitance (see 2.6.1) modifies the ZVS region as a function of V_{in} and coupling k. For low couplings and high power, the best results are obtained for primary capacitances as high as $750\,\mathrm{pF}$. For nominal coupling $k = 0.135$, the optimum primary capacitance is emperically determined as $560\,\mathrm{pF}$. As a consequence it is almost impossible to have the inverter operating in soft-switching.
- When v_{gs} goes high, v_{ds} should be zero. However, oscilations are popping up caused by common-source inductance embedded in the switch. Additional inductance in the gate-driver enforces this.

With the component values from table 8.1, the in-, output power and efficiency were simulated for the coupling factor ranging from 0.01 to 0.15. The results are plotted in figure 7.4b. The highest simulated efficiency is 90%

at $k = 0.15$. The drain-source voltage waveform as well as the drain current are plotted in respectively figure 7.5a and 7.5b. The system remains close to soft-switching, but the variation of coupling is enough to push the system in early ZVS, making the system a lot lossier. A more realistic simulation with $0.12 \leq k \leq 0.15$ as to identify the influence of misalignment results in output powers of respectively $850\,\mathrm{W}$ to $1250\,\mathrm{W}$ and efficiencies ranging from 89.3% to 89.5%.

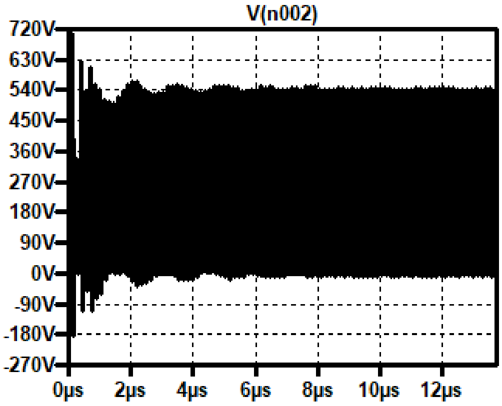

***(a)** Ringing v_{ds} at transient startup*

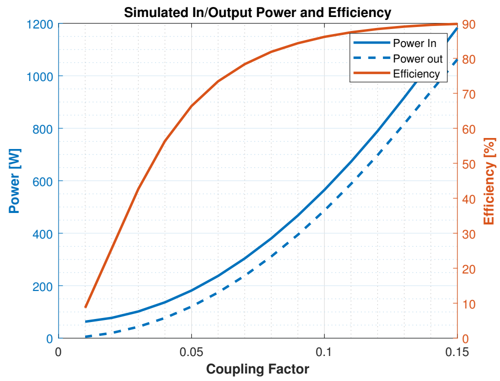

***(b)** In/Output power and efficiency*

***Figure 7.4:** Simulated transient v_{ds} response and input-, output power and efficiency*

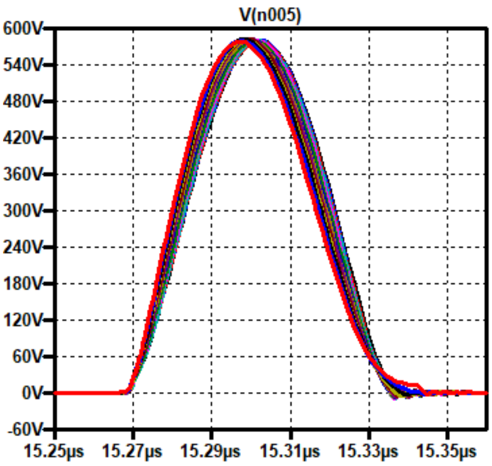

***(a)** v_{ds}*

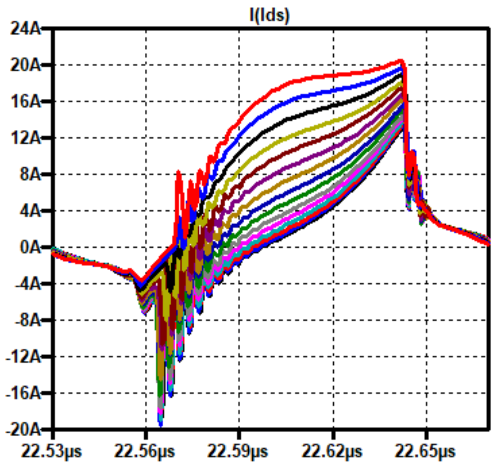

***(b)** i_d*

***Figure 7.5:** Simulated waveforms when sweeping k*

Chapter 8

Results

Data resulting from measurements on the demonstrator is supplied in this chapter. First, a series of experiments verified the square loop self inductance and coupling factors. The second part highlights the steady state behavior of the system.

8.1 Equipment

The experiments were performed with a KeySight impedance analyzer, model E4990A. A calibrated extension cable, 16046G, was attached to the analyzer to connect to a test fixture, 16047E. Before doing the measurements, the correct calibration procedure was conducted with RF calibration resitor E4990-61051. Low power tests were conducted with a 3-channel programmble power supply, the Rohde&Schwarz HMP2030.

8.2 Loop Inductance

To determine whether the laser-cutted rectangular copper loop matches the FEM simulations, a series of experiments were done. Both self and mutual inductance are measured without ferrite shielding below the loop and with ferrite shielding at 1 mm and 5 mm.

8.2.1 Component Values

Table 8.1 lists the realized component values.

L_{in}	442 nH	$L_0 + L_{P1}$	1.07 µH
L_{S2}	201 nH		
C_{in}	560 pF	C_0	600 pF
C_P	4.4 nF	C_S	4.4 nF
GaN FET	GS66508B	**SiC Diode**	STPSC406D
Ferrite Shield	Wurth 364003		

Table 8.1: *Component values*

8.2.2 Self Inductance

The self-inductances were measured with an impedance analyzer. The measurements clearly show the beneficial effect of ferrite on the self-inductance. The closer the ferrite shield, the higher the inductance. However, the ferrite should have negligible losses up to 10 MHz according to the datasheet. This is proven incorrect as the Q-factor is highest with an air core (see table 8.2 and figure 8.1).

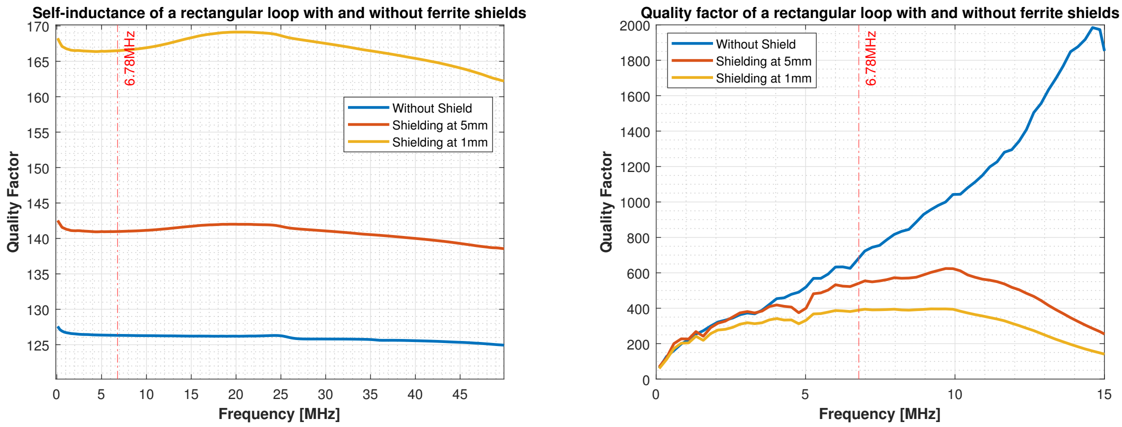

***(a)** Self Inductance*   ***(b)** Quality Factor*

***Figure 8.1:** Measurement results without ferrite shielding, and shielding at* $5\,\mathrm{mm}$ *and* $1\,\mathrm{mm}$

	Inductance [nH]	**Quality Factor**	**R** [mΩ]
Without Shield	126.3	675	7.98
Shielding at $1\,\mathrm{mm}$	166.5	388	18.3
Shielding at $5\,\mathrm{mm}$	141.0	538	11.2

***Table 8.2:** Measured self-inductances and quality factors for a single rectangular loop in air at* $6.78\,\mathrm{MHz}$

8.2.3 Coupling Factor

The coupling between the coils was measured at various distances. To do so, both coils were set at the correct distance apart after which the self inductance of the primary was measured for both open- and shorted secondary. The coupling factor is a derived quantity based on expression 8.1 with $L_{P,shorted}$ the primary inductance for a shorted secondary and $L_{P,open}$ the primary inductance for an open secondary. Interestingly, when the shielding plate is at $5\,\mathrm{mm}$, the coupling is consistently higher compared to an air core in the range of interest. However, with a shield at $1\,\mathrm{mm}$, the best coupling is obtained for the smallest separation distances. In terms of coupling, the best overall performance is therfore obtained with a ferrite shield at $5\,\mathrm{mm}$. These statements are made based on figure 8.2.

$$k = \sqrt{1 - \frac{L_{P,shorted}}{L_{P,open}}} \tag{8.1}$$

With the ferrite added to the system, the resonator becomes twice as lossy. For this reason, it was decided to conduct the other experiments without it. To obtain coupling factors close to simulation, the pads are moved closer together.

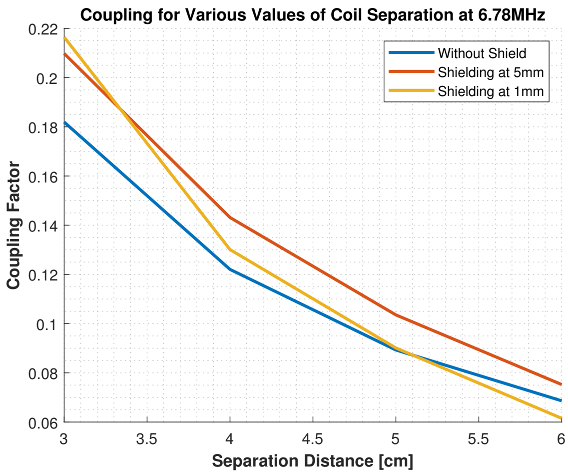

Figure 8.2: *The coupling between the two coils for various separation distances at* 6.78 MHz

8.3 Full System Test

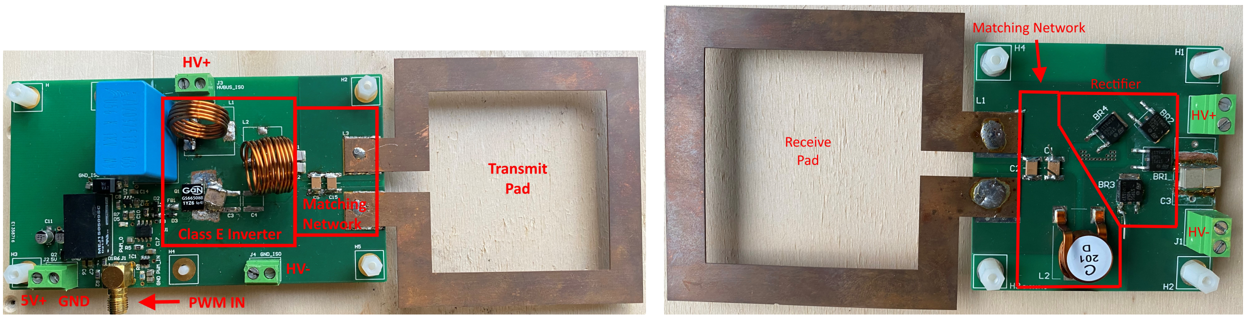

(a) *Transmitter*

(b) *Receiver*

Figure 8.3: *Transmitter and receiver PCBs*

The transmitter and receiver PCBs are visible in figure 8.3. Several system blocks are highlighted for clarity. Both are made on a dual sided PCB with a FR-4 dielectric of 1.5 mm thickness. The schematic files as well as PCB layout are supplied in appendix D.

During the experiments, several modifications were necessary to improve the original design:

- A ferrite bead in the gate driver was replaced by a shunt
- The input capacitor was placed too far from the switch, resulting in oscillations. In figure 8.3a the capacitor is moved closer.
- Placed a heatsink on the bottom side and cooled it actively (for safety)
- The DC film capacitor at the receiver output was replaced by a ceramic capacitor

First of all, during testing it proved difficult to enter soft-switching mode. At some point, it was discovered that a schottky diode connected to the gate, which is responsible for discharging, had a faulty footprint. Fixing this bug made it possible to enter soft switching, but only for a fixed input voltage. This was verified for $k = 0$ (operating without secondary) and was found to be 42 V. This value was found by probing the v_{gs} and v_{ds} waveforms and also by looking at the dissipated power, which was lowest at 42 V. The total loss was then 6.2 W, which is already higher than the expected loss of 4.2 W according to simulations. Above this value the systems suffers from early ZVS as is visible in figure 8.4a. This resulted in an increase of power dissipation up to 15 W at 50 V input. Several tests were done in which the input voltage was increased up to 80 V, no soft switching was witnessed. The total power dissipation would increase to $22\,\mathrm{W}$. With the secondary coupled soft switching was not possible.

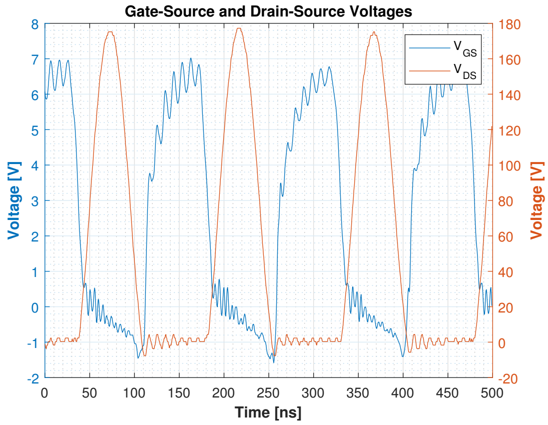

(a) Gate-source (blue) and drain-source (orange) waveforms at $6.78\,\mathrm{MHz}$ with $V_{in} = 50\,\mathrm{V}$

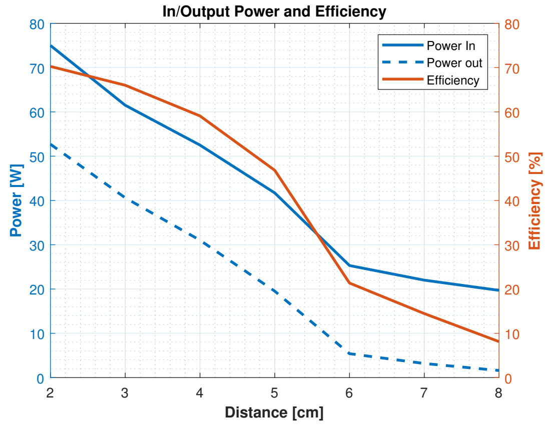

(b) Power and efficiency curves

***Figure 8.4:** Switching waveforms without secondary and in-, output power and efficiency*

The transmitted power was also measured at several separation distances for $V_{in} = 50\,\mathrm{V}$. The resulting, in- and output power as well as the DC-DC efficiency are supplied in figure 8.4b. The maximum efficiency of 70% is obtained for a separation distance of only $2\,\mathrm{cm}$. The transmitted power is lower than would be expected from the secondary. The output power drops of almost linearly with distance, which is also unexpected as it should be quadratic. The change in slope at $6\,\mathrm{cm}$ separation distance is expected since the coupling drops rapidly when the air-gap becomes larger than the coil size.

During testing the thermals were monitored with an IR camera. Three clear heat hotspots popped up, namely the switch itself, the input inductor and the capacitors in parallel with the loop inductor. The capacitors would both heat up quickly due to the large current ripple, which was not part of the initial selection procedure. The picture also shows both capacitors heating up separately, which is a sign of current sharing, which is good as there were worries one capacitor might process most current. The capacitors were in this case the bottleneck. The maximum temperature would increase beyond the measurable range of the IR camera, as can be seen in figure 8.5.

Figure 8.5: *Thermal image of the transmitter*

Chapter 9

Conclusions and recommendations

9.1 Discussion

From the start this research was set out as empirical work. The idea was to develop an understanding of the field and analyze, simulate and design a WPT system. The design would only be validated for its theoretical validity and target performance (expected efficiency and output power). If this was achieved, the design would be tested in practice to test for incosistencies in the design.

Although this approach is not always the best and certainly not cheapest, it is a relatively quick way in power electronics to gather information and find gaps in your own knowledge as well as mistakes in your design, especially since good component models are scarce. The only problem with this approach is incorrectable mistakes in your hardware. Fixing these can be time consuming and is a hazard with only limited time.

The above mentioned disadvange is true for this work. The PCB was designed incorrectly causing a lot of wasted time in simultions and the lab. The hardware was faulty due to a mistake in an earlier simulation model, but mainly inexperience of the author. Together, these resulted in an unfixable system. A few of these misconceptions were:

- Large currents are no problem when low loss components are used
- Smaller capacitors have less parasitics
- Capacitors can handle any ripple current as long as maximum voltage does not exceed the maximum ratings
- A capacitor tolerance of 5% is sufficient to get a working prototype
- Thermal modelling of capacitors is unneccesary

This resulted in a system that is not even close to operating according to the requirements. Both output power as well as efficiency are way below on what is expected. The causes of these defficiencies are believed to be:

- The inverter is hard-switched most of the time
- The components cannot handle the large current or current ripple (or both)
- The resonant networks are detuned

It is believed the effect of C_{oss} was bigger in the realized end-product compared to simulations [35]. A possible explanation is an improper soldering joint. Although this would not directly influence C_{oss}, increased heating of the switching device could do so. Increased C_{oss} does explain why the inverter is only soft-switched for a particular voltage.

Large currents with significant ripple content limit the design and decrease the performance. Only self-made air core inductors are applicable for such high ripples. Especially when the PCB is not initially designed for this, tuning difficulties arise where the inductance is not consistent across the desired operating window. Additionally, severe ripple content is a cause for overheating of capacitors causing them to age quicker as well as detune the system even more. Better system performance is only possible when the ripple is within the limits of the capacitor.

Another major cause of the detuned system are the capacitors with tolerances of 5%. The only way of matching the capacitor was to measure it. With standard inductances having tolerances of 20% the task of matching them properly becomes daunting.

9.2 Conclusions

With the emergence of wide-bandgap semiconductors a lot of possibilities have popped up for WPT to increase the output power and efficiency, whilst decreasing the system cost, weight and size. Current research is mostly focussing on high power transfers with a focus on:

- Operation at high switching frequencies, 6.78 MHz and 13.56 MHz
- New inverter layouts to decrease current and voltage stresses on the components as well as losses
- Other inverter solutions to operate load-independently
- High-Q resonators

A thorough analysis of S-S, LCL-P and LCL-LCL resonant networks was presented in the context of an inductively coupled system. The LCL-P resonant network was quickly found to be a special case of LCL-LCL and was not applicable to this application. Eventually an LCL-LCL topology was picked as best option to work in conjunction with the load-independent inverter.

The design and simulation to derive at an optimum coupler in terms of the requirements is presented. The design was parametrized to iterate quickly through possible solutions. The expected coupling was expected to be around 0.135 with a high-frequency ferrite used for shielding. A symmetrical resonator is preferred for the highest coupling. The experimental results indicate a lower coupling factor (0.105) and show a severe loss when ferrites are added to the system.

Circuit simulations of the full design have shown efficiencies of up to 90% at 1.2 kW at the desired operating window. The effect of detuning was simulated and qualitatively studied. Minor imperfections have shown to have significant impact on the resulting performance. Especially detuning of the secondary is a major concern where for any detuning case the performance decreases.

The theoretical design was realized and matched against simulations. The practical system behaved very differently compared to the one that was simulated. The major cause for lower efficiency is hard-switching, whereas the major cause for decreased output power is detuning. Additionally, several component were found to overheat. Extra investigation has showed assumptions in component characteristics resulted in a flawed PCB design. The experiments have shown a maximum efficiency of 70% with a power output of 52 W.

9.3 Recommendations

9.3.1 System Design

The high currents through the input inductor and the antenna LC tanks is currently a limiting factor in the design. Decreasing the currents would reduce the losses quadratically and improve thermal performance. Potential second order effects such as detuning are then less likely to occur as well. To decrease the currents, the voltage must obviously go up, which is not possible with the current inverter layout because it is already operating at maximum input voltage. Two possible changes are proposed:

- Move to a push-pull inverter to double the voltage across the resonant tank.
- Move to a different inverter such as EF_2 or even ϕ_2. These have lower voltage stress across the switch and higher voltages.

Especially the push-pull option can be profitable because the ripple content significantly reduces as well. However, the required load resistance as seen by load-independent class E inverter goes up.

9.3.2 PCB Design

For easier testing it is required to modify the PCB. The following modifications are advised:

- Include proper testpoints to measure v_{GS}, v_{DS}
- Include drain current shunt to measure i_D
- Use a design with shielded inductors (more realistic for EMC/EMI tests)
- Add a trimmer capacitance
- Add testpoints at the input/output of the resonant network to measure the impedance
- Move to a 4-layer PCB

With these modifications gathering data as well as tuning become a lot easier.

9.3.3 Future Research

The major flaw of current megahertz WPT systems is the necessity of low component tolerances. This becomes even more difficult for increased powers as the number of components on the market decreases. To improve the odds of commercialization as well as system performance future research should try to find ways to automatically tune the system. Other improvements can be made in the resonator structures where it is believed that very high Q links can be realized.

Bibliography

[1] J. Heath. “Mutual inductance and transformers: When emf becomes emi”. J. Heath, Ed. (Apr. 13, 2017), [Online]. Available: https://www.analogictips.com/mutual-inductance-transformers-emf-becomes-emi/.

[2] J. Agbinya, *Wireless Power Transfer, 2nd Edition*. Aalborg: River Publishers, 2015, ISBN: 9788793237636.

[3] L. Efthymiou, G. Camuso, G. Longobardi, T. Chien, M. Chen, and F. Udrea, “On the source of oscillatory behaviour during switching of power enhancement mode GaN HEMTs”, vol. 10, no. 3, p. 407, 2017. DOI: 10.3390/en10030407.

[4] L. Gu, G. Zulauf, A. Stein, P. A. Kyaw, T. Chen, and J. M. R. Davila, “6.78-MHz wireless power transfer with self-resonant coils at 95% DC–DC efficiency”, *IEEE Transactions on Power Electronics*, vol. 36, no. 3, pp. 2456–2460, 2021. DOI: 10.1109/tpel.2020.3014042.

[5] N. Mohan, T. M. Undeland, and W. P. Robbins, *Power Electronics: Converters, Applications, and Design*. IEEE COMPUTER SOC PR, Oct. 1, 2002, 832 pp., ISBN: 0471226939. [Online]. Available: https://www.ebook.de/de/product/3799992/ned_mohan_tore_m_undeland_william_p_robbins_power_electronics_converters_applications_and_design.html.

[6] D. M. Robert W. Erickson, *Fundamentals of Power Electronics*. Springer International Publishing, Aug. 16, 2020, 1104 pp., ISBN: 3030438791. [Online]. Available: https://www.ebook.de/de/product/38632090/robert_w_erickson_dragan_maksimovi_fundamentals_of_power_electronics.html.

[7] A. Lidow, M. de Rooij, J. Strydom, D. Reusch, and J. Glaser, *GaN transistors for efficient power conversion*. John Wiley & Sons, Mar. 30, 2020, 386 pp., ISBN: 1119594146. [Online]. Available: https://www.ebook.de/de/product/36062414/alex_lidow_michael_de_rooij_johan_strydom_david_reusch_john_glaser_gan_transistors_3e.html.

[8] P. Clayton, *Introduction to Electromagnetic Compatibility*. John Wiley & Sons, Dec. 22, 2005, pp. 342–342, 1014 pp., ISBN: 0471755001. [Online]. Available: https://www.ebook.de/de/product/5176958/paul_compatibility_2e_w_website.html.

[9] F. Fiorillo, C. Beatrice, O. Bottauscio, and E. Carmi, “Eddy-current losses in mn-zn ferrites”, *IEEE Transactions on Magnetics*, vol. 50, no. 1, pp. 1–9, 2014. DOI: 10.1109/tmag.2013.2279878.

[10] N. Tesla, “Apparatus for transmitting electrical energy”, U.S. Patent US1119732A, 1907. [Online]. Available: https://patents.google.com/patent/US1119732A/en.

[11] J. Boys, “Inductive power transfer across an extended gap”, European pat. EP1010229A4, 1998. [Online]. Available: https://patents.google.com/patent/EP1010229A4.

[12] A. Kurs, A. Karalis, R. Moffatt, J. D. Joannopoulos, P. Fisher, and M. Soljacic, “Wireless power transfer via strongly coupled magnetic resonances”, *Science*, vol. 317, no. 5834, pp. 83–86, 2007. DOI: 10.1126/science.1143254.

[13] A. Karalis, J. Joannopoulos, and M. Soljačić, “Efficient wireless non-radiative mid-range energy transfer”, *Annals of Physics*, vol. 323, no. 1, pp. 34–48, 2008. DOI: 10.1016/j.aop.2007.04.017.

[14] M. Kiani and M. Ghovanloo, "The circuit theory behind coupled-mode magnetic resonance-based wireless power transmission", *IEEE Transactions on Circuits and Systems I: Regular Papers*, vol. 59, no. 9, pp. 2065–2074, 2012. DOI: 10.1109/tcsi.2011.2180446.

[15] A. P. Sample, D. A. Meyer, and J. R. Smith, "Analysis, experimental results, and range adaptation of magnetically coupled resonators for wireless power transfer", *IEEE Transactions on Industrial Electronics*, vol. 58, no. 2, pp. 544–554, 2011. DOI: 10.1109/tie.2010.2046002.

[16] B. L. Cannon, J. F. Hoburg, D. D. Stancil, and S. C. Goldstein, "Magnetic resonant coupling as a potential means for wireless power transfer to multiple small receivers", *IEEE Transactions on Power Electronics*, vol. 24, no. 7, pp. 1819–1825, 2009. DOI: 10.1109/tpel.2009.2017195.

[17] C. Cai *et al.*, "Design and optimization of load-independent magnetic resonant wireless charging system for electric vehicles", *IEEE Access*, vol. 6, pp. 17 264–17 274, 2018. DOI: 10.1109/access.2018.2810128.

[18] J. Jadidian and D. Katabi, "Magnetic MIMO", in *Proceedings of the 20th annual international conference on Mobile computing and networking*, ACM, 2014. DOI: 10.1145/2639108.2639130.

[19] S. Jayalath and A. Khan, "Design, challenges, and trends of inductive power transfer couplers for electric vehicles: A review", *IEEE Journal of Emerging and Selected Topics in Power Electronics*, pp. 1–1, 2020. DOI: 10.1109/jestpe.2020.3042625.

[20] R. Bosshard, U. Iruretagoyena, and J. W. Kolar, "Comprehensive evaluation of rectangular and double-d coil geometry for 50 kW/85 kHz IPT system", *IEEE Journal of Emerging and Selected Topics in Power Electronics*, vol. 4, no. 4, pp. 1406–1415, 2016. DOI: 10.1109/jestpe.2016.2600162.

[21] M. A. de Rooij, "The zvs voltage-mode class-d amplifier, an egan fet-enabled topology for highly resonant wireless energy transfer", in *2015 IEEE Applied Power Electronics Conference and Exposition (APEC)*, IEEE, 2015. DOI: 10.1109/apec.2015.7104562.

[22] H. Koizumi, M. Iwadare, S. Mori, and K. Ikeda, "A class d type high frequency tuned power amplifier with class e switching conditions", IEEE, 1994. DOI: 10.1109/iscas.1994.409312.

[23] H. Koizumi, T. Suetsugu, M. Fujii, K. Shinoda, S. Mori, and K. Iked, "Class DE high-efficiency tuned power amplifier", vol. 43, no. 1, pp. 51–60, 1996. DOI: 10.1109/81.481461.

[24] N. Sokal and A. Sokal, "Class e-a new class of high-efficiency tuned single-ended switching power amplifiers", vol. 10, no. 3, pp. 168–176, 1975. DOI: 10.1109/jssc.1975.1050582.

[25] F. Raab, "Idealized operation of the class e tuned power amplifier", vol. 24, no. 12, pp. 725–735, 1977. DOI: 10.1109/tcs.1977.1084296.

[26] M. Acar, A. Annema, and B. Nauta, "Generalized design equations for class-e power amplifiers with finite DC feed inductance", IEEE, 2006. DOI: 10.1109/eumc.2006.281237.

[27] J. M. Rivas, Y. Han, O. Leitermann, A. D. Sagneri, and D. J. Perreault, "A high-frequency resonant inverter topology with low-voltage stress", *IEEE Transactions on Power Electronics*, vol. 23, no. 4, pp. 1759–1771, 2008. DOI: 10.1109/tpel.2008.924616.

[28] Z. Kaczmarczyk, "High-efficiency class e,ef2, and e/f3 inverters", *IEEE Transactions on Industrial Electronics*, vol. 53, no. 5, pp. 1584–1593, 2006. DOI: 10.1109/tie.2006.882011.

[29] R. Zulinski and K. Grady, "Load-independent class e power inverters. i. theoretical development", *IEEE Transactions on Circuits and Systems*, vol. 37, no. 8, pp. 1010–1018, 1990. DOI: 10.1109/31.56074.

[30] S. Aldhaher, D. C. Yates, and P. D. Mitcheson, "Load-independent class e/EF inverters and rectifiers for MHz-switching applications", *IEEE Transactions on Power Electronics*, vol. 33, no. 10, pp. 8270–8287, 2018. DOI: 10.1109/tpel.2018.2813760.

[31] L. Zhang, "Load-independent class-e power conversion", English, Ph.D. dissertation, Virginia Tech, Apr. 13, 2020. [Online]. Available: `http://hdl.handle.net/10919/97601` (visited on 09/23/2021).

[32] S. Kee, I. Aoki, A. Hajimiri, and D. Rutledge, "The class-e/f family of ZVS switching amplifiers", vol. 51, no. 6, pp. 1677–1690, 2003. DOI: `10.1109/tmtt.2003.812564`.

[33] S. Aldhaher, G. Kkelis, D. C. Yates, and P. D. Mitcheson, "Class ef2 inverters for wireless power transfer applications", in *2015 IEEE Wireless Power Transfer Conference (WPTC)*, IEEE, 2015. DOI: `10.1109/wpt.2015.7140141`.

[34] S. Aldhaher and P. D. Mitcheson, "500w 13.56mhz class EF push-pull inverter for advanced dynamic wireless power applications", in *2019 IEEE PELS Workshop on Emerging Technologies: Wireless Power Transfer (WoW)*, IEEE, 2019. DOI: `10.1109/wow45936.2019.9030603`.

[35] J. Choi, D. Tsukiyama, Y. Tsuruda, and J. M. R. Davila, "High-frequency, high-power resonant inverter with eGaN FET for wireless power transfer", *IEEE Transactions on Power Electronics*, vol. 33, no. 3, pp. 1890–1896, 2018. DOI: `10.1109/tpel.2017.2740293`.

[36] C. H. Kwan, J. M. Arteaga, D. C. Yates, and P. D. Mitcheson, "Design and construction of a 100 w wireless charger for an e-scooter at 6.78 MHz", in *2019 IEEE PELS Workshop on Emerging Technologies: Wireless Power Transfer (WoW)*, IEEE, 2019. DOI: `10.1109/wow45936.2019.9030648`.

[37] C. H. Kwan, J. M. Arteaga, S. Aldhaher, D. C. Yates, and P. D. Mitcheson, "A 600w 6.78mhz wireless charger for an electric scooter", in *2020 IEEE PELS Workshop on Emerging Technologies: Wireless Power Transfer (WoW)*, IEEE, 2020. DOI: `10.1109/wow47795.2020.9291303`.

[38] C. Kwan, "Design of wireless power transfer systems in the presence of living objects", Ph.D. dissertation, 2018.

[39] J. Li and D. Costinett, "Comprehensive design for 6.78 MHz wireless power transfer systems", in *2018 IEEE Energy Conversion Congress and Exposition (ECCE)*, IEEE, 2018. DOI: `10.1109/ecce.2018.8557513`.

[40] K. Surakitbovorn and J. Rivas-Davilla, "Design of a GaN-based wireless power transfer system at 13.56 MHz to replace conventional wired connection in a vehicle", in *2018 International Power Electronics Conference (IPEC-Niigata 2018 -ECCE Asia)*, IEEE, 2018. DOI: `10.23919/ipec.2018.8507473`.

[41] L. Kalpoe, "Exploration of the possibilities of wireless power transfer for e-bikes and business opportunities", M.S. thesis, 2020. [Online]. Available: `http://essay.utwente.nl/82303/`.

[42] K. Cartwright, E. Joseph, and E. Kaminsky, "Finding the exact maximum impedance resonant frequency of a practical parallel resonant circuit without calculus", *Technology Interface International Journal*, vol. 11, pp. 26–36, 2010.

[43] D. Voglitsis, V. Prasanth, T. Todorcevic, and P. Bauer, "Theoretical analysis and experimental investigation of high frequency bidirectional CPT system", in *2014 IEEE Transportation Electrification Conference and Expo (ITEC)*, IEEE, 2014. DOI: `10.1109/itec.2014.6861771`.

[44] Z. Zhang, H. Pang, A. Georgiadis, and C. Cecati, "Wireless power transfer—an overview", *IEEE Transactions on Industrial Electronics*, vol. 66, no. 2, pp. 1044–1058, 2019. DOI: `10.1109/tie.2018.2835378`.

[45] T. Imura, *Wireless Power Transfer*. Springer-Verlag GmbH, Jun. 16, 2020. [Online]. Available: `https://www.ebook.de/de/product/39267886/takehiro_imura_wireless_power_transfer.html`.

[46] Y. Yang, J. Cui, and X. Cui, "Design and analysis of magnetic coils for optimizing the coupling coefficient in an electric vehicle wireless power transfer system", *Energies*, vol. 13, no. 16, p. 4143, 2020. DOI: `10.3390/en13164143`.

[47] C. Paul, *Inductance : loop and partial*. Hoboken, N.J. Piscataway, N.J: Wiley IEEE, 2010, ISBN: 9780470561232.

[48] M. A. Houran, X. Yang, and W. Chen, “Magnetically coupled resonance WPT: Review of compensation topologies, resonator structures with misalignment, and EMI diagnostics”, *Electronics*, vol. 7, no. 11, p. 296, 2018. DOI: 10.3390/electronics7110296.

[49] M. H. Nguyen and H. F. Blanchette, “Optimizing AC resistance of solid PCB winding”, *Electronics*, vol. 9, no. 5, p. 875, 2020. DOI: 10.3390/electronics9050875.

[50] R. Steigerwald, “A comparison of half-bridge resonant converter topologies”, vol. 3, no. 2, pp. 174–182, 1988. DOI: 10.1109/63.4347.

[51] G. Zulauf, S. Park, W. Liang, K. N. Surakitbovorn, and J. Rivas-Davila, “COSS losses in 600 v GaN power semiconductors in soft-switched, high- and very-high-frequency power converters”, *IEEE Transactions on Power Electronics*, vol. 33, no. 12, pp. 10 748–10 763, 2018. DOI: 10.1109/tpel.2018.2800533.

[52] C.-S. Wang, G. Covic, and O. Stielau, “Power transfer capability and bifurcation phenomena of loosely coupled inductive power transfer systems”, *IEEE Transactions on Industrial Electronics*, vol. 51, no. 1, pp. 148–157, 2004. DOI: 10.1109/tie.2003.822038.

Appendix A

Self Wound Air Core Inductors

The original input and filter inductors are too lossy at $6.78\,\mathrm{MHz}$. This was already expected, but the core material and losses were not accurately described within the datasheet. During low-power tests, they would already heat up significantly. During later tests, it was discovered that Coilcraft provides a web-page where it is possible to play around with different cores versus ripple currents. It was quickly confirmed that indeed the core losses are excessive. Additionally, none of the other products by Coilcraft provided the desired solution as the ripple current is significant.

To determine the appropriate inductor dimensions, `https://hamwaves.com/inductance/en/index.html#input` was used to make a first estimate. The inductor was measured with an impedance analyzer when wound. The values that were used in the online calculator as well as the results at $6.78\,\mathrm{MHz}$ are summarized in table A.1. The results from the impedance analyzer are supplied for completeness in figure A.1.

	L_{in}	L_{filter}
Wire Diameter [mm]	1	1
Wire Material	Copper	Copper
Inductor Diameter [mm]	15	15
Turns	5	10
Length [mm]	5.5	10.5
Theoretical Inductance [nH]	417	1,007
Measured Inductance [nH]	442	1,070
Theoretical Q	79	92
Measured Q	143	183

Table A.1: *Inductor parameters and characteristics for self wound air-core inductors*

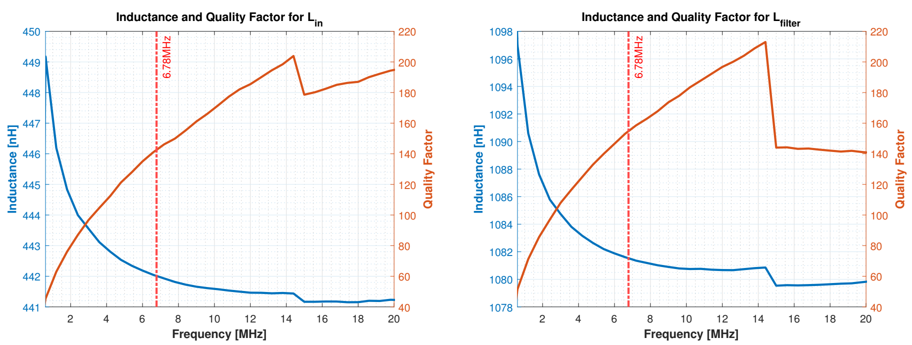

(a) *L_{in} Inductance and Q-factor*

(b) *L_0 Inductance and Q-factor*

Figure A.1: *Inductances and quality factors for self wound air-core inductors*

Appendix B

LTSpice Model Files

The models made in LTSpice are supplied here.

B.1 LCL-LCL

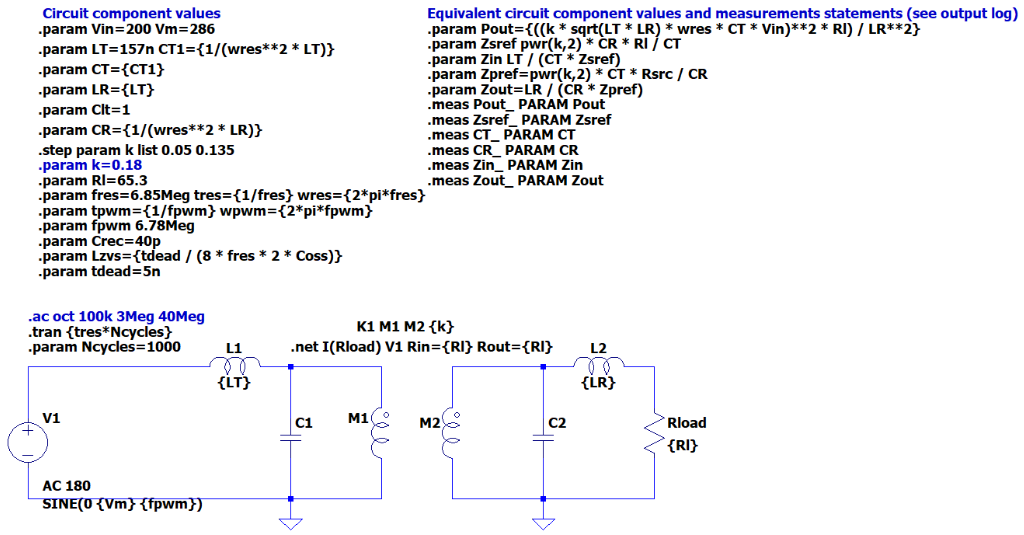

Figure B.1: *LCL-LCL LTSpice model*

B.2 Class E Inverter

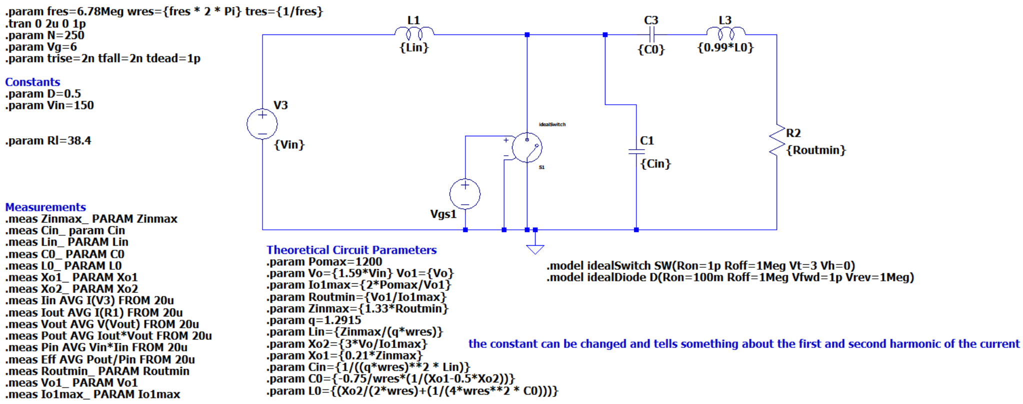

Figure B.2: *Class E inverter LTSpice model*

B.3 Full System

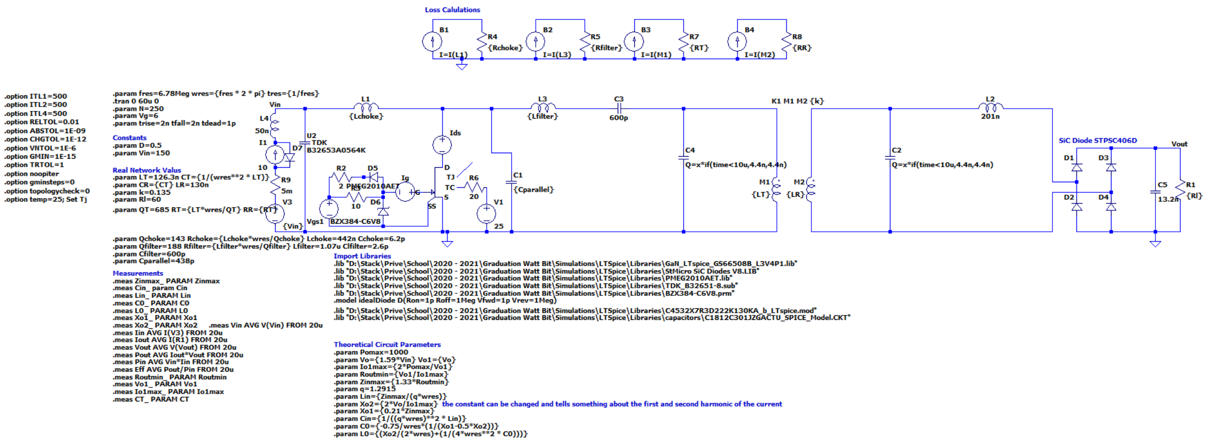

Figure B.3: *Full system LTSpice model*

Appendix C

Load Independent Class E Inverter

The expressions for I_{ini}, i_{in}, v_{ds} and i_{Cin} valid for $0 \leq t \leq 0.5T_s$ are supplied here for convenience [31].

$$\begin{aligned}
I_{ini} &= \frac{V_{in}\sin q\pi - V_{in}q^2\sin q\pi + I_{o1}Z_{in}\sin\theta + I_{o1}Z_{in}q\sin q\pi\cos\theta}{Z_{in}\cos q\pi\,(q^2-1)} + \frac{q^2}{q^2-1}I_{o1}\sin\theta \\
&= -\frac{V_{in}\sin q\pi}{Z_{in}\cos q\pi} + I_{o1}\sin\theta\frac{1}{q^2-1}\frac{1+q^2\cos q\pi}{\cos q\pi} + I_{o1}\frac{q\sin q\pi\cos\theta}{\cos q\pi\,(q^2-1)}
\end{aligned} \tag{C.1}$$

$$\begin{aligned}
i_{in}(t) = &\left[-\frac{V_{in}\sin q\pi}{Z_{in}\cos q\pi} + I_o\sin\theta\frac{1}{q^2-1}\frac{1+q^2\cos q\pi}{\cos q\pi} + I_o\frac{q\sin q\pi\cos\theta}{\cos q\pi\,(q^2-1)}\right]\cos(q\omega_s t) \\
&+ I_o\frac{q}{q^2-1}\sin(\omega_s t+\theta_1) - I_o q\frac{q\cos(q\omega_s t)\sin\theta + \sin(q\omega_s t)\cos\theta}{q^2-1} + \frac{V_{in}}{Z_{in}}\sin(q\omega_s t)
\end{aligned} \tag{C.2}$$

$$\begin{aligned}
v_{ds}(t) = &Z_{in}\left[\sin\theta\frac{1}{q^2-1}\frac{1+q^2\cos q\pi}{\cos q\pi} + \frac{q\sin q\pi\cos\theta}{\cos q\pi\,(q^2-1)}\right]I_o\sin(q\omega_s t) \\
&+ \frac{qZ_{in}}{(q^2-1)}I_o\cos\theta\cos q\omega_s t - \frac{q^2Z_{in}}{(q^2-1)}I_o\sin(q\omega_s t)\sin\theta \\
&- \frac{qZ_{in}}{(q^2-1)}I_o\cos(\omega_s t+\theta) + 2V_{in}\sin^2\left(\frac{q\omega_s t}{2}\right) - \frac{V_{in}\sin q\pi}{\cos q\pi}
\end{aligned} \tag{C.3}$$

$$\begin{aligned}
i_{Cin}(t) = &I_o\frac{q}{q^2-1}\left(\frac{\sin\omega_s t}{q} - \sin q\omega_s t - \frac{\sin q\pi\cos q\omega_s t}{1-\cos q\pi}\right) \\
&+ \frac{V_{in}}{Z_{in}}\left(\frac{q\pi+\sin q\pi}{1-\cos q\pi}\cos q\omega_s t + \sin q\omega_s t\right)
\end{aligned} \tag{C.4}$$

Appendix D

Layout Files

D.1 Circuit Design

D.1.1 Transmitter

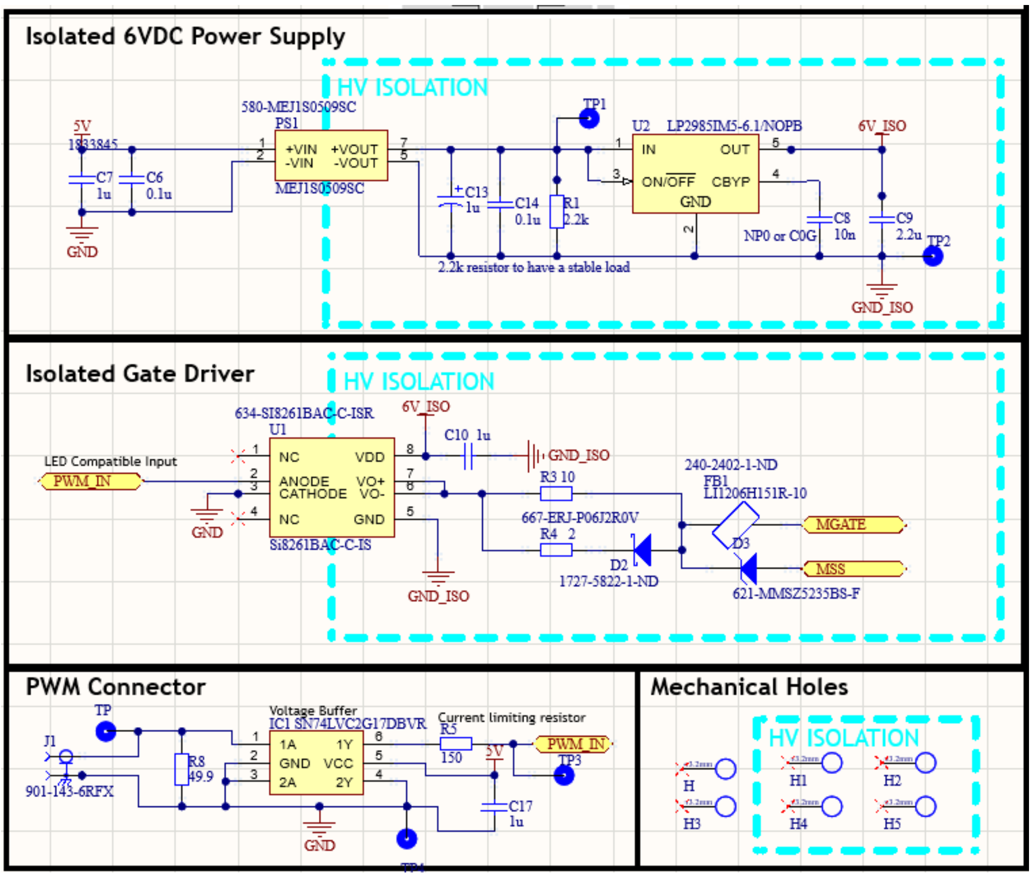

Figure D.1: Transmitter schematic design 1/2

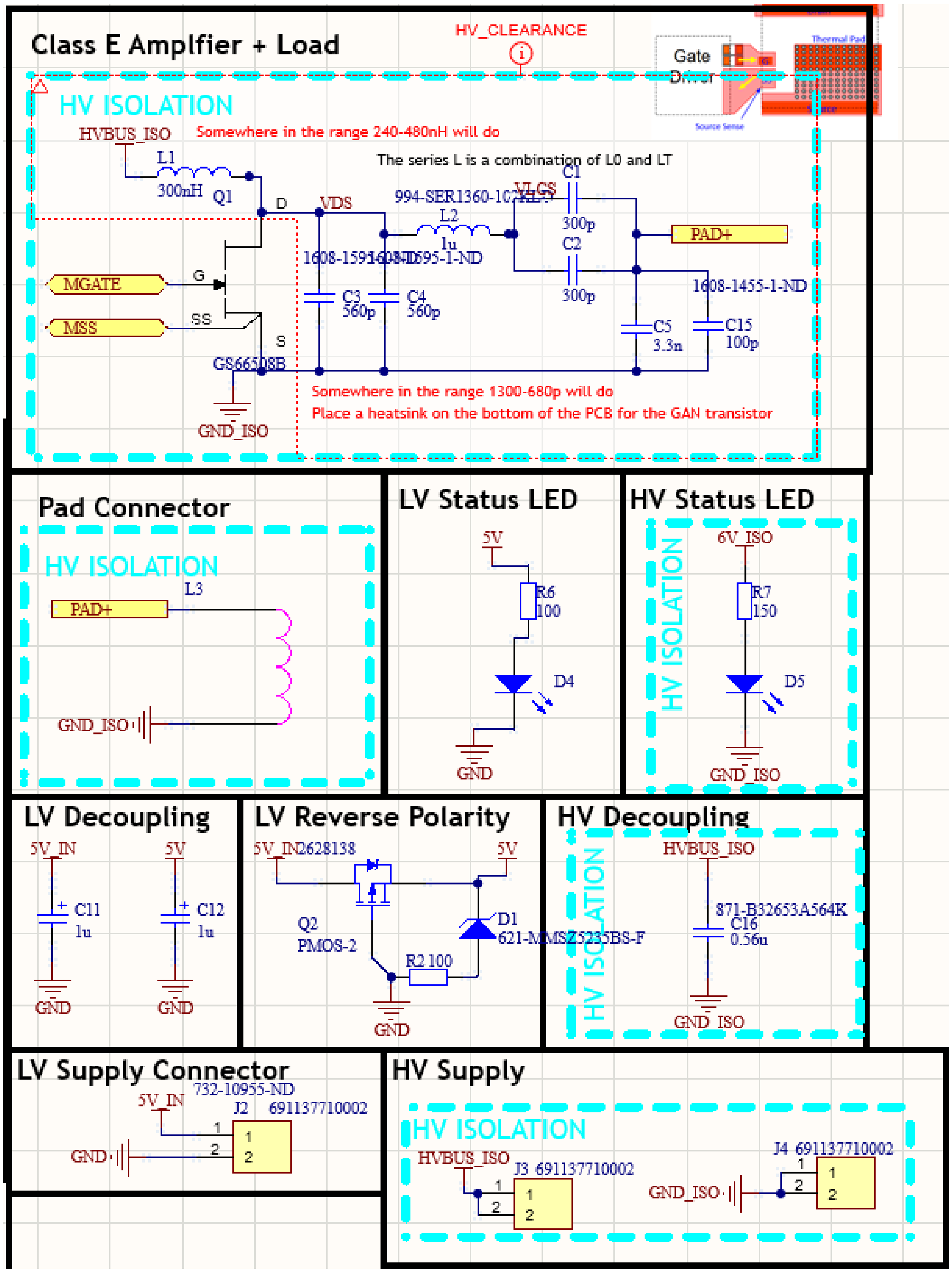

Figure D.2: *Transmitter schematic design 2/2*

D.1.2 Receiver

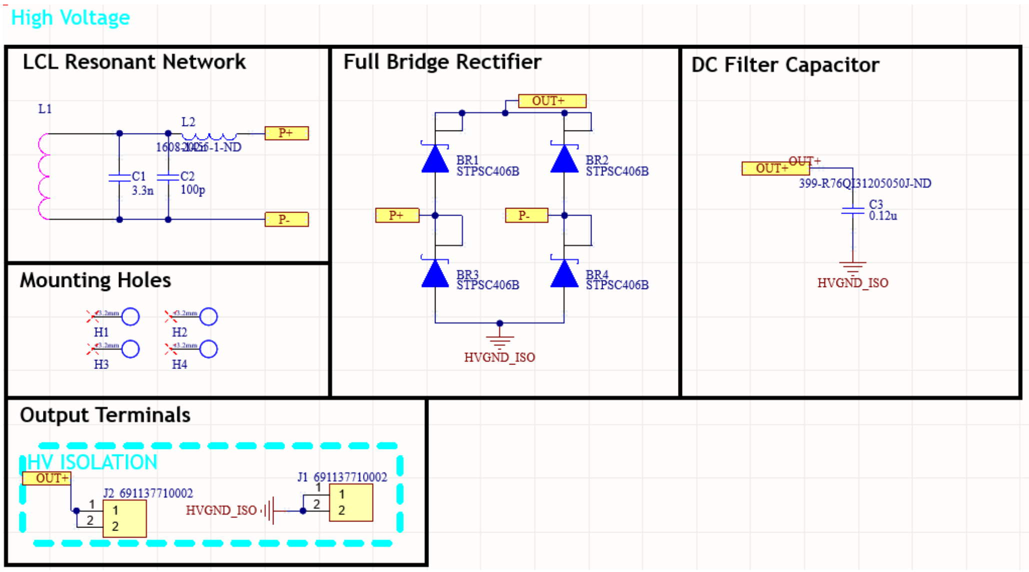

Figure D.3: *Receiver schematic design*

D.2 PCB Layout

D.2.1 Transmitter

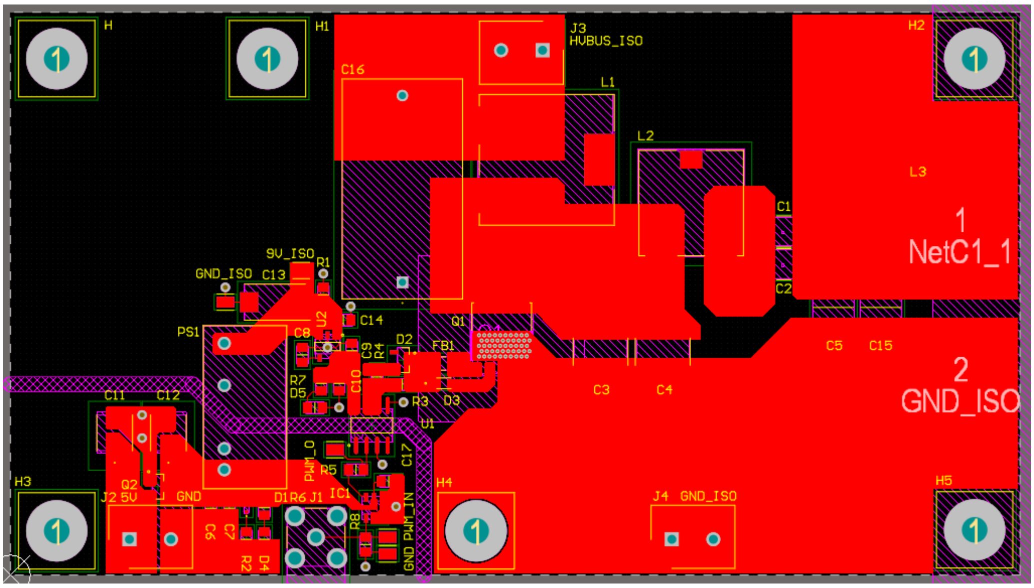

(a) Transmitter PCB Top Layer

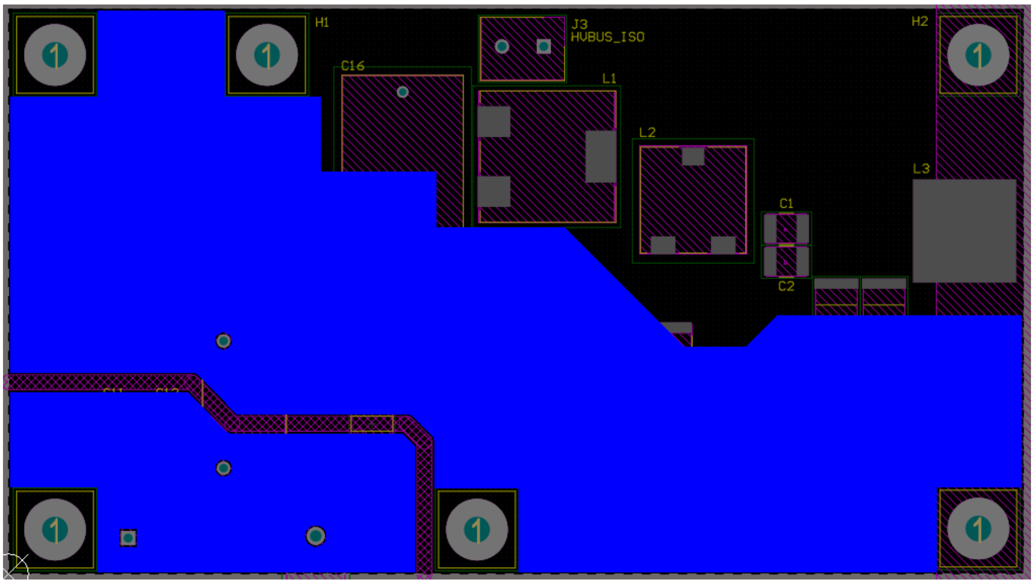

(b) Transmitter PCB Bottom Layer

D.2.2 Receiver

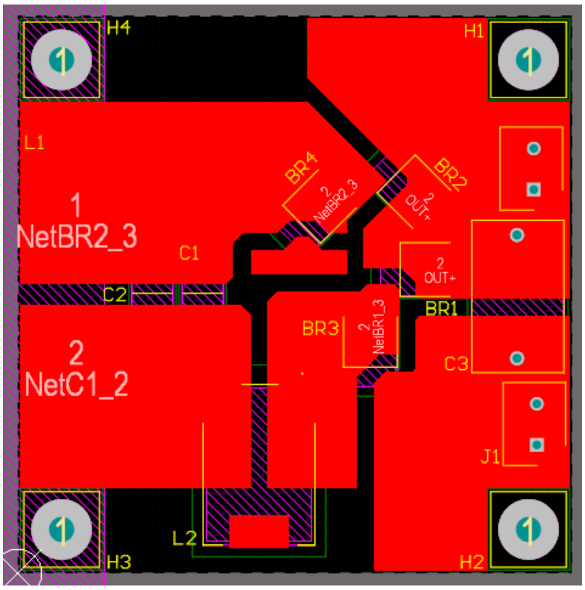

(a) Receiver PCB Top Layer

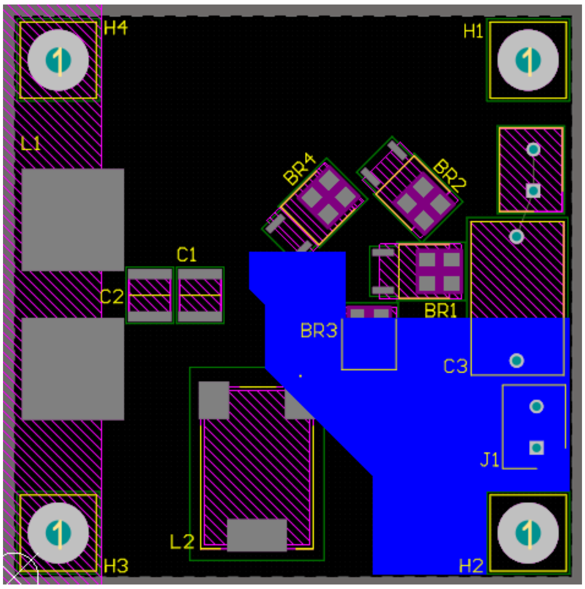

(b) Receiver PCB Bottom Layer